



Optimizing Thermal-Optical Methods for Measuring Atmospheric Elemental (Black) Carbon: A Response Surface Study

Joseph M. Conny, Donna B. Klinedinst, Scott A. Wight, and Jeffrey L. Paulsen

Surface and Microanalysis Science Division, National Institute of Standards and Technology, Gaithersburg, Maryland

The chemical, physical, and morphological complexity of atmospheric aerosol elemental carbon (EC) presents major problems in assuring measurement accuracy. Since EC and black carbon are often considered equivalent, methods based on thermal-optical analysis (TOA) are widely used for EC in ambient air samples because no prior knowledge of the aerosol's absorption coefficient is required. Nevertheless, different TOA thermal desorption protocols result in wide EC-to-total-carbon (TC) variation. We created three response surfaces with the following response variables: EC/TC, maximum laser attenuation in the He phase (L_{\max}), and laser attenuation at the end of the He phase (L_{He4}). A two-level central-composite factorial design comprised of four factors considered the temperatures and durations of all desorption steps in TOA's inert (He) phase and the initial step in TOA's oxidizing (O_2 -He) phase. L_{\max} was used to assess the positive bias caused by nonvolatile unpyrolyzed organic carbon (OC char) being measured as native EC. A negative bias that the attenuated laser response does not detect is caused by the loss of native EC in the He phase. L_{He4} was used as a surrogate indicator for the loss of native EC in the He phase. The intersection between the L_{\max} and L_{He4} surfaces revealed TOA conditions where both the production of OC char in the He phase was maximized and the loss of native EC in the He phase was minimized, therefore leading to an optimized thermal desorption protocol. Based on the sample types used in this study, the following are generalized optimal conditions when TOA is operated in the fixed-step-durations, laser-transmission mode (i.e., TOT): step 1 in He, 190°C for 60 s; step 2 in He, 365°C for 60 s; step 3 in He, 610°C for 60 s; step 4 in He, 835°C for 72 s. For steps 1–4 in O_2 -He, the conditions are 550°C

for 180 s, 700°C for 60 s, 850°C for 60 s, and 900°C for 90 s to 120 s, respectively.

INTRODUCTION

Atmospheric elemental carbon (EC) is a ubiquitous component of particulate matter $<2.5 \mu\text{m}$ in aerodynamic diameter (PM_{2.5}) and appears at measurable levels in even the most remote locations (Hopper et al. 1994; Wolff and Cachier 2002). It is a persistent product of incomplete combustion, principally of fossil fuels in transportation, heating, power generation, and industrial processes, wood for residential heating, and agricultural biomass (primarily in the tropics). Natural wildfires in the temperate and boreal zones are also significant EC sources. The prevalence of aerosol EC has been a concern because of its suspected deleterious effect on health and agriculture, its effect on visibility, and its effect on climate change via the solar radiation budget. Long-term exposure to combustion-related aerosols in the most polluted urban areas has been linked to an increased risk of mortality from lung cancer (Pope et al. 2002), a health risk comparable to long-term exposure to second-hand smoke.

Measurement of atmospheric aerosol EC has long been problematic, due largely to the fact that its chemical, physical, and morphological nature is complex and quite variable. The terms graphitic carbon or black carbon (BC) are commonly used synonymously with EC. Regardless of terminology, these species are refractory and consist of insoluble sheetlike polycyclic carbon structures that wrap around each other to form nodules (or primary particles) of around 10 nm to 30 nm in diameter (Seinfeld and Pandis 1998; Watson and Valberg 2001). As the nodules form, they also typically cluster to form aggregated particles of sizes from 0.1 μm to 1 μm or more. As with graphite, the oxidation state of carbon in the aggregates is close to zero. EC combined with organic carbon (OC) and inorganic substances on particles from combustion forms soot. Variation in fuel and conditions of combustion, however, results in considerable variation

Received 1 November 2002; accepted 13 March 2003.

The authors would like to express appreciation for the efforts of George A. Klouda of NIST and Helen Parish of SRI in providing the urban PM samples, and John F. Slater of the University of New Hampshire for assistance in sampling forest fire emissions. We also thank David L. Duerwer of NIST for helpful discussions on the factorial design. This work was supported in part by the U.S. Environmental Protection Agency through an interagency agreement on aerosol metrology with the NIST.

Address correspondence to Joseph M. Conny, Surface and Microanalysis Science Division, National Institute of Standards and Technology, 100 Bureau Drive, Stop 8371, Gaithersburg, MD 20899. E-mail: joseph.conny@nist.gov

in the chemical composition of aggregated soot particles as well as their size, shape, and physical properties (Watson and Valberg 2001).

The chemical and morphological complexity of EC aerosols has led to a lack of consensus on the exact nature of the analyte. EC complexity and the wide scope of measurement methodologies (e.g., optical, photoacoustic, thermal, chemical, and thermal with optical) have led researchers to conclude that EC is defined operationally by the measurement method. We make a distinction in definition, however, between EC and BC. Excluding nonrefractory humic OC and inorganic substances such as iron that may contribute to light absorption by the aerosol, BC is the refractory carbon component of PM that absorbs visible light at a specified wavelength. Since the term EC does not necessarily imply optical dependence, atmospheric aerosol EC is operationally defined at this state of the science and is best described as graphite-like, but it is not carbon in either of its pure elemental forms. For the purposes of this work, we define EC as BC.

For the determination of EC mass as BC, several long-established methods rely on the analyte's optical behavior, either absorptive or reflective. Most optical methods were originally developed to measure aerosol optical extinction, in particular the absorption coefficient. For example, the integrating plate (IP), integrating sphere, and IP variants (Campbell et al. 1995; Clarke 1982; Hitzenberger et al. 1996; Lin et al. 1973) measure extinction of longer-wave visible light through a particle-laden filter. Extinction from the filter substrate is subtracted, and scattering is minimized by various instrument fixes or empirical correction factors. Continuous EC monitoring is achieved with the aethelometer (Hansen et al. 1984) or particle soot absorption photometer (Bond et al. 1999), in essence a continuous IP using a filter substrate.

These optical methods have also been used for inexpensive and rapid EC mass measurement based on Beer's Law and optical absorptivity. Success here depends on the constancy of the light attenuation per unit EC mass (i.e., specific attenuation) (Gundel et al. 1984) and ultimately on knowledge of the contributions of the aerosol scattering and absorption coefficients to the specific attenuation. Since these methods rely solely on the optical nature of the aerosol, accuracy of the absorption coefficient is critical. However, aerosols from different locations or measured at different times from the same location may have sharply different optical properties. For example, Hitzenberger (1993) reported that the absorption coefficient of aerosol collected during wintertime in Vienna was six times higher than that for aerosol collected during summertime.

There are a number of causes for variation in the absorption coefficient that are unrelated to instrument bias or imprecision. For one, the absorption coefficient is proportional to an ensemble of the photon capture cross-sections of multiple poorly characterized EC species in a polydisperse aerosol sample. Since the relative proportions of EC compounds, as well as the total EC mass, vary from site to site, the aerosol absorption coefficient

necessarily varies from site to site or with the time of sampling. In addition, the absorption coefficient is affected by the optical properties of other chemical species in the sample. EC-containing particles in ambient air can be externally mixed with compositionally different particles that primarily scatter light, in particular sulfate, nitrate, and organic compounds such as polycyclic aromatic hydrocarbons (PAHs). However, EC may also be mixed with light-scattering species within individual particles (internal mixture). In this case, the absorption coefficient is dependent upon the average particle refractive index, which itself is a function of the refractive indexes of the nonabsorbing particle matrix as well as the absorber. Aerosols that contain internally mixed particles exhibit a larger absorption coefficient than aerosols consisting of a mixture of chemically distinct particles (Ackerman and Toon 1981).

There is, therefore, a conundrum in applying optical properties alone to quantify both EC mass and the varying aerosol absorptivity upon which mass measurement relies. A solution is to combine thermal desorption with optical extinction, i.e., thermal-optical analysis (TOA) (Huntzicker et al. 1982; Johnson et al. 1981). In TOA, carbonaceous material in particles deposited on a quartz-fiber filter is thermally desorbed in several temperature stages that can range from 120°C to 900°C among various TOA methods. A continuous gas stream carries the desorbed carbonaceous material through an oxidizer (typically a tube containing MnO₂ at 870°C or 912°C), which efficiently converts organic carbon to CO₂. The CO₂ can be detected directly, e.g., by nondispersive infrared spectroscopy, or indirectly, by reduction to CH₄ followed by flame ionization detection. Before and during heating, the optical behavior of the filter is monitored from the attenuation in laser light (typically 633 nm or 670 nm), either as transmission through the filter, the TOT method (Birch 1998; Birch and Cary 1996), or as reflection from it, the TOR method (Chow et al. 1993). In an inert gas stream such as helium desorption of the more thermally stable organic compounds typically occurs at lower temperatures (around 300°C or less), while thermally unstable organic compounds typically pyrolyze at higher temperatures, and can produce "char" on the filter that further attenuates the laser light. The char is removed from the filter in an oxidizing gas stream—typically O₂ in He—later in the analysis and then measured in the same way as the thermally stable carbon. As the temperature in the oxidizing stream rises, the attenuated laser signal (transmission or reflectance) eventually returns to the attenuated laser signal of the filter prior to thermal desorption. The time when the laser response returns to the initial response is called the split point: the critical point where native EC is "split" analytically from char. Char is assumed to have approximately the same absorptivity as native EC. Therefore, regardless of where char and EC actually come off the filter in the oxidizing gas stream, any desorbed carbon mass beyond the split point is measured as native EC. TOA methods monitor the optical properties of the sample, but do not utilize the absorption coefficient to determine EC mass. Since a priori knowledge of the absorption

coefficient is not required, TOA is preferred for measuring EC mass over purely optical methods. The TOT method has a long history of use by the U.S. EPA and is currently used for the EPA's PM_{2.5} speciation network. The TOR method has been used with the Interagency Monitoring of Protected Visual Environments (IMPROVE) sampling network to measure EC on >100,000 PM_{2.5} and PM₁₀ samples (Malm et al. 1994).

TOT and TOR often produce varying EC results for the same sample material. For example, measurements on NIST SRM 1649a distributed on quartz-fiber filters showed EC to total carbon (TC) ratios of 0.20 and 0.26 for the TOT method and 0.43 for the TOR method (Currie et al. 2002). One reason for measurement discrepancies is the fact that for PM imbedded in a fibrous substrate absorption and reflectance of the char produced during heating are not, in practice, complementary properties. Nevertheless, the major reason for varying TOT and TOR results is the use of different thermal desorption protocols. As TOT and TOR evolved, their protocols diverged in the temperature and duration of the desorption steps. TOT commonly employs the protocol for the NIOSH 5040 method (Birch 1998; Birch 1999) or slight modifications thereof (e.g., Cary 1994); TOR commonly employs the IMPROVE protocol developed by the Desert Research Institute (Chow et al. 1993; Chow et al. 2001). Table 1 summarizes the differences between the two desorption protocols. Both methods desorb thermally stable compounds and pyrolyze the remaining OC in a single He phase. In addition, both methods oxidize the pyrolyzed OC and native EC in a single O₂-He phase with 1% to 2% O₂. The methods differ to a greater extent in the temperature and duration of steps as compared to their number. The NIOSH 5040 protocol has higher step temperatures overall. For example, the second step temperature in the He phase for the NIOSH 5040 protocol (500°C)

is midway between the third and fourth He-phase steps for the IMPROVE protocol. However, defining differences between the two protocols are perhaps exhibited in the first and last He-phase steps. The first NIOSH temperature on the Celsius scale is more than twice the corresponding IMPROVE temperature, while the last NIOSH temperature is 300°C higher than the corresponding IMPROVE temperature. Step duration for the IMPROVE protocol varies and depends on the width of the FID peak that evolves at a particular desorption step. A step ends when the peak returns to baseline, typically 1 min to 2 min into the step. In contrast, step duration is fixed for the NIOSH protocol but increases from the first step to last in both the He phase and O₂-He phase.

In this work, response-surface methods were used to optimize the TOA thermal desorption protocol for EC accuracy. Accuracy in this case is elusive because a comprehensive understanding of the chemical nature of EC is still lacking. In addition, the critically important process of separating instrument-produced OC char from native EC is operationally difficult because the char is assumed to be chemically similar to native EC. Nevertheless, we approach this task by addressing two hypotheses. First, non-absorbing OC that does not volatilize or char in He is measured erroneously as EC during the O₂-He phase, causing a positive bias. Among the thermal methods, OC is known to carry over into the EC fraction and overestimate EC by as much as a factor of 50 (Novakov and Corrigan 1995). Thus, optimal production of char in He is necessary. Second, if loss of char occurs at high temperature and the laser response does not adjust accordingly, an unaccountable loss of native EC may also occur because of the chemical similarity of char and native EC. The result in this case is a negative bias. To assess the extent of the positive and negative biases we modeled the laser attenuation through the filter as the OC was pyrolyzed.

Table 1
IMPROVE and NIOSH thermal-desorption protocols for TOA

	Step	IMPROVE (TOR) ^{1,2}	NIOSH 5040 (TOT) ³	Magnitude of temperature difference
He phase	1	120°C	250°C (≈325°C) ⁴ for 1 min	130°C
	2	250°C	500°C for 1 min	250°C
	3	450°C	650°C for 1 min	200°C
	4	550°C	850°C for 1.5 min	300°C
O ₂ -He phase	1	550°C	650°C for 0.5 min	100°C
	2	700°C	750°C for 0.5 min	50°C
	3	800°C	850°C for 1 min	50°C
	4		940°C for 2 min	

¹From Chow et al. 1993.

²Step duration for the IMPROVE protocol is variable. It is determined by the width of the FID signal peak that appears during the desorption step. The step ends when the peak returns to baseline.

³From Birch 1998.

⁴On the first thermal optical carbon analyzers manufactured by Sunset Labs, the actual oven temperature for a particular desorption step was higher than the set point used with the instrument software when the set point was <500°C. Thus, the NIOSH 5040 method was commonly run with a temperature for the first desorption step that was substantially higher than the published temperature associated with the method.

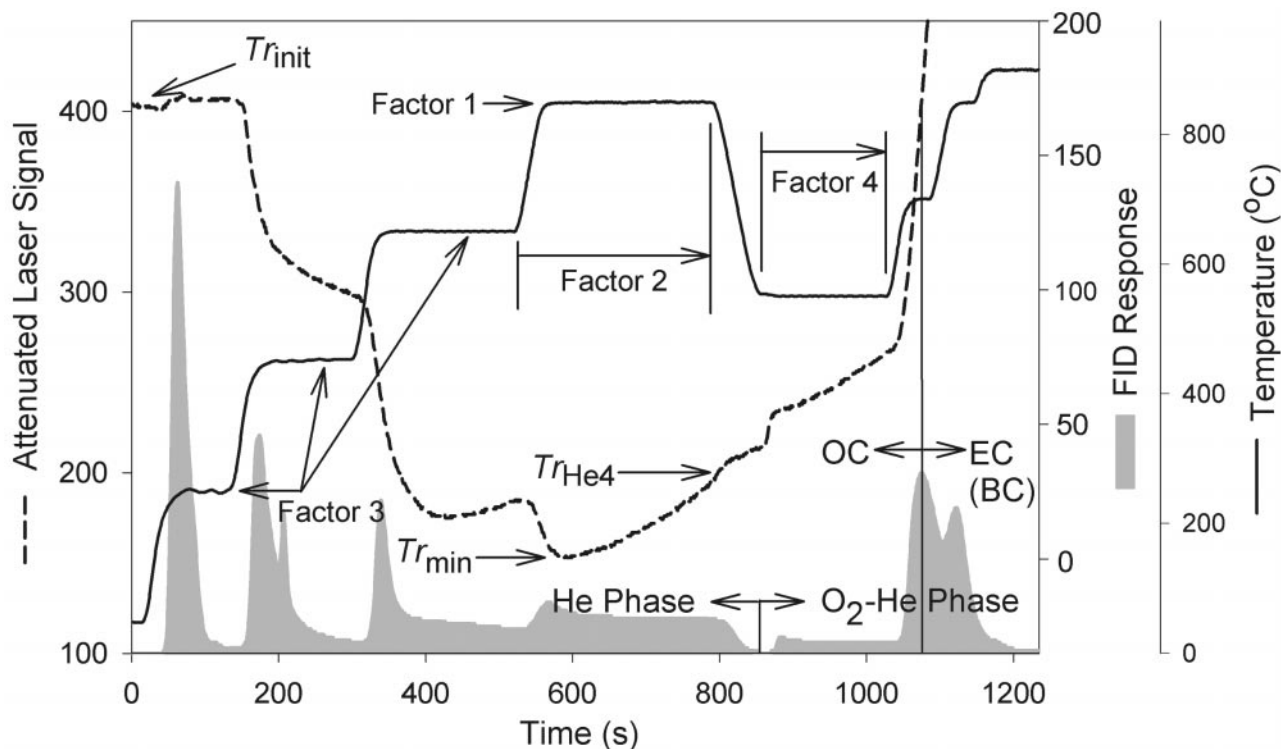


Figure 1. TOA thermogram from an analysis on lab air particles showing the temperature profile (solid line), laser transmission through filter at 670 nm (dashed line), and FID signal (shaded area). Also shown is the boundary between the inert He phase and oxidizing O₂-He phase, the split point, and factors in the central-composite factorial design. Factor 1 is the temperature of step 4 in He, factor 2 is the duration of step 4 in He (with steps 1–3 varied proportionately), factor 3 is the temperatures of steps 1–3 varied in concert, and factor 4 is the duration of step 1 in O₂-He. $T_{r_{init}}$ is the attenuated laser signal prior to carbon desorption, $T_{r_{min}}$ is the attenuated laser signal at its minimum, and $T_{r_{He4}}$ is the attenuated laser signal at the end of the He phase.

Three types of samples were studied to represent indoor ambient air, outdoor ambient air, and a carbonaceous aerosol source. To determine conditions for thermal desorption, we employed a central-composite factorial design (Massart et al. 1988). Among the 7–8 desorption steps in the IMPROVE or NIOSH protocols, there are 14–16 factors to account for both temperature and duration that can be used to assess the TOA response. In a central composite design, this would result in 16,413 to 65,569 factor combinations! To make the task more manageable, we identified four factors associated with the step temperature and duration that would likely have the greatest impact on variation in the EC/TC ratio. However, this required that individual step temperatures and durations be combined, as described below. The selection of the factors was based in part on prior work (Chow et al. 2001) that determined that the fourth He-phase temperature, i.e., the highest temperature used to pyrolyze OC, was largely responsible for differences in the TOT and TOR methods. With this in mind, four factors were used in the design (Figure 1): (1) temperature of step 4 in He, (2) duration of steps 1–4 in He, (3) temperature of steps 1–3 in He (varied proportionately), and (4) duration of step 1 in O₂-He.

METHODS

The Sunset Laboratories' Thermal Optical Carbon Analyzer employing the TOT method was used to measure OC and EC on three sample types.* To represent ambient indoor air, particles <0.95 μm in aerodynamic diameter in laboratory air were collected on a precleaned 20 cm \times 25 cm quartz-fiber filter positioned as the after-filter in a Staplex Hi-Vol 4-Stage Cascade Impactor. 1.5 cm² punches from the filter were taken for analysis following a randomized and blocked sampling protocol. Filter-edge versus filter-center variation due to particle deposition inhomogeneities was determined by analysis of variance (ANOVA), and corrections were made to minimize sampling bias. To represent ambient outdoor air, fine particles (<2.5 μm diameter) of the NIST Urban Dust Standard Reference Material (SRM 1649a) were separated from bulk material using impactors and then resuspended on precleaned 37 mm quartz-fiber filters

*Certain commercial products are identified here to specify the means by which experiments were conducted. Such identification is not intended to imply recommendation or endorsement by the National Institute of Standards and Technology, nor is it intended to imply that the identified product is necessarily the best available for the purpose.

(Klouda et al. 1996; Klouda 2002). SRM 1649a is an outdoor PM that was collected in large quantities in Washington, DC during 1976–1977 using filter bags. The material was passed through a 125 μm sieve to remove extraneous materials including bag fibers. It is believed to typify urban PM (NIST 2001). To represent a carbonaceous aerosol source, fine particles from the smoldering stage of a boreal forest fire were collected on a precleaned 20 cm \times 25 cm quartz-fiber filter positioned in the fine-particle stream of an MSP Model 310 Virtual Impactor (Conny and Slater 2002). While the smoldering forest fire sample used here does not represent aerosol from forest fires in general, it nevertheless was useful in this study because it exhibited pronounced charring in TOA, as evidenced below, compared to the other two samples. The lab air and urban PM samples had similar amounts of total carbon, averaging $29.89 \pm 0.37 \mu\text{g C cm}^{-2}$ ($\bar{x} \pm tsn^{1/2}$, $t = 2$, $n = 48$) and $28.24 \pm 1.09 \mu\text{g C cm}^{-2}$ ($n = 30$), respectively. The smoldering fire sample had $53.93 \pm 0.65 \mu\text{g C cm}^{-2}$ ($n = 26$). Carbonate was not detected in either the ambient air samples or the smoldering fire sample.

Figure 1 is a thermogram showing, as a function of analysis time, the desorption temperature (solid line), transmission of 670 nm light through a quartz-fiber filter (dashed line), and FID response (shaded area). The time delay between the attenuated laser response and the FID response (hence, the transit time for carbon to reach the FID), determined just prior to conducting experiments, was 6 s. Consistent with both the TOT and TOR methods, we used a single He phase (Compressed He purity 99.9999%, Scott Specialty Gases, Plumsteadville, PA, USA) to desorb thermally stable compounds and pyrolyze the remaining organic carbon. We used a single O₂-He phase (1.0% O₂ volume fraction) to oxidize the pyrolyzed OC and native EC. Also consistent with the TOT and TOR methods, we employed four temperature steps in the He phase. These temperatures varied with the factorial design as described below. Four fixed temperature steps were used in the O₂-He phase (550°C, 700°C, 850°C, and 900°C); the first two are equivalent to those in the IMPROVE protocol and the third step is equivalent to that in the NIOSH protocol. The temperature at the start of analyses was maintained at approximately 50°C.

Factorial Design

The factorial design was a composite of two parts: a two-level full factorial design consisting of 16 (2^k , $k =$ number of factors) combinations and a partial two-level star factorial design consisting of 9 ($2k + 1$) combinations, for a total of 25 combinations. (For a comprehensive introduction to factorial designs, see Box et al. 1978). The complete design is shown graphically in Figure 2. The two solid-line cubes arranged vertically in the figure represent the full factorial. Their placement along the main vertical axis corresponds to the two factor 1 temperature levels, 550°C and 850°C. The three axes of each cube represent factors 2–4. Imbedded between the two full-factorial

cubes is the corresponding star figure with the three dashed-line axes representing factors 2–4. The center of the star in this figure coincides with the factor 1 temperature at 700°C. Filled circles represent levels of the full-factorial and the open circles represent levels of the star factorial. Included at each factor combination is the symbolic code used in subsequent figures and explanations. For example, (+ + + +) represents the full-factorial combination where all factors are at the upper level; (+ + - -) represents the full-factorial combination where factors 1 and 2 are at the upper level and factors 3 and 4 are at the lower level; and (/ / + /) represents the star factorial combination where factors 1, 2, and 4 are at the central level and factor 3 is at the upper level.

Factor 1. Factors were selected and ordered to the extent that they were expected to contribute to EC/TC variation and accuracy (Figure 1). The temperature of step 4 in He was assigned factor 1 because it was expected to have the largest effect on both OC charring and on the loss of native EC, due perhaps to adventitious oxidation in the presence of a substance in the sample with a higher reduction potential than EC. The two levels for this factor in the full factorial corresponded to the step temperatures of the IMPROVE and NIOSH protocols, 550°C and 850°C, respectively. For the lower and upper levels of the star factorial, we used 500°C and 900°C, i.e., 50°C below and above the IMPROVE and NIOSH protocols, respectively. The star center level was the midpoint: 700°C. Levels of each factor for the full factorial and star factorial are shown in Table 2.

Factor 2. Related to the effect of step temperature on EC/TC is step duration. Hence, He-step duration was expected to have the next largest effect and was assigned factor 2. We focused primarily on the He step 4 duration. The two levels for this duration in the full factorial were 1.5 min and 4.5 min; the former is the duration from the NIOSH protocol. The lower and upper star factorial levels were 1 min and 5 min; the star center level was the midpoint at 3 min. Scaling the durations of steps 1–3 to the duration of step 4 was necessary to make these steps consistent with step 4 as TOA might typically be run. The duration of step 1 was 1 min and 2 min, respectively, for the lower and upper levels of both the full factorial and the star factorial; the center level for the star factorial was 1.5 min. In each case, the duration of steps 2 and 3 were spaced proportionately as shown in Table 2. For example, when the He step 4 duration was 1.5 min, steps 1–3 were 1 min, 1.17 min, and 1.33 min, respectively. When the He step 4 duration was 4.5 min, steps 1–3 were 2 min, 2.8 min, and 3.7 min, respectively.

Factor 3. Just as the temperature of step 4 in He likely affects EC/TC, the temperatures of steps 1–3 also might affect it. To account for their effect, we varied these step temperatures as a group. In our design, we used 125°C and 250°C for the two levels of the step 1 temperature in the full factorial, which correspond roughly to the He step 1 temperatures for the IMPROVE and NIOSH protocols, respectively. For the star factorial levels, we used 100°C, 188°C, and 325°C. The temperatures of steps 2 and 3 were scaled proportionately as the step 4 temperature was

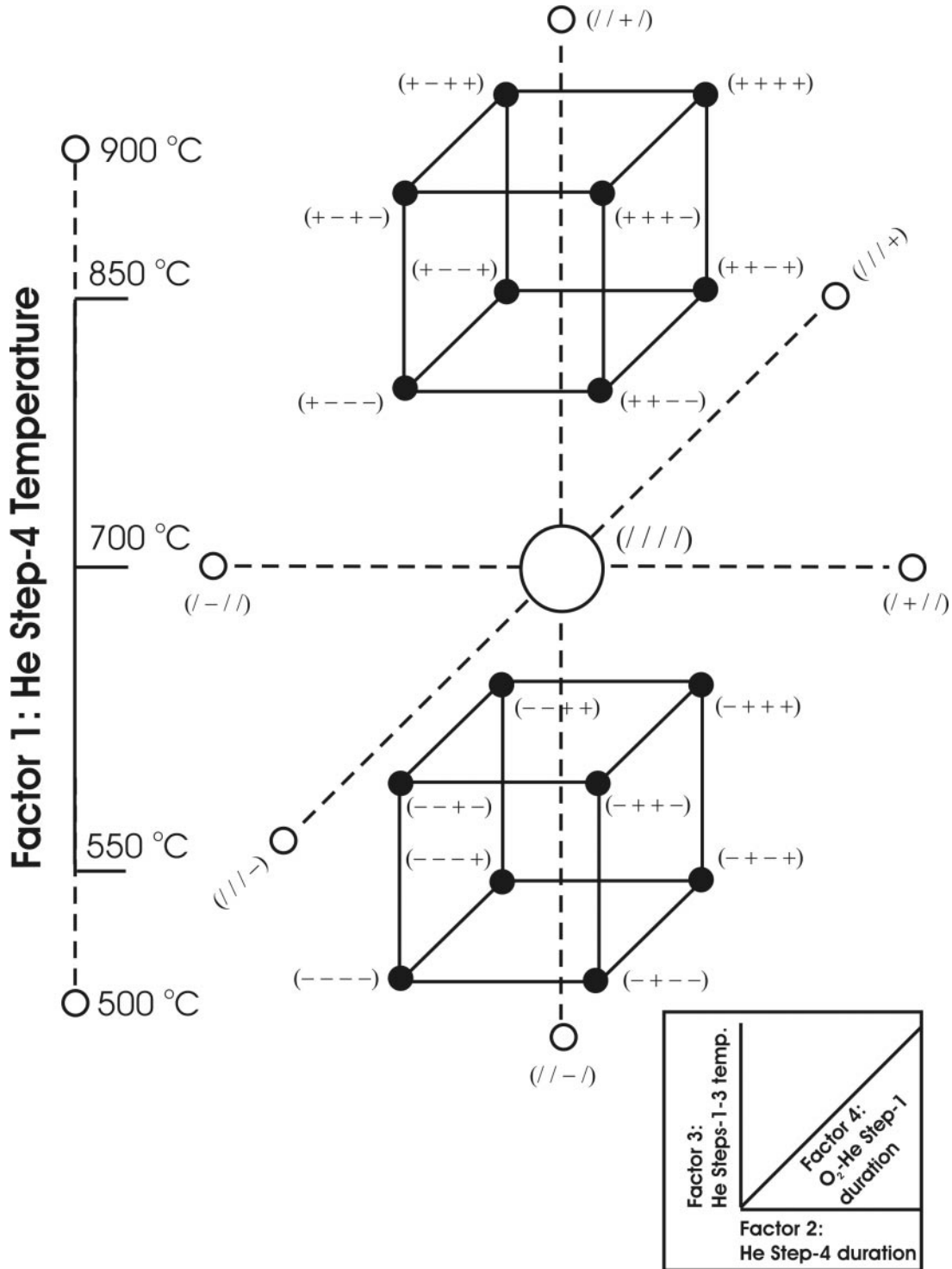


Figure 2. Graphical representation of the two-level full factorial design and the two-level partial (star) factorial design that comprise the central-composite factorial design used to set parameters for the various TOA thermal desorption experiments. The two cubes represent the four factors for the full factorial. The upper cube and lower cubes each represent the 8 full-factorial combinations associated with the upper and lower levels, respectively, of factor 1. The 16 total combinations of the full-factor are represented by the closed circles with the four-symbol code that indicates the upper (+) or lower (–) level of factors 1–4 as indicated in Table 2. The star represents the central partial factorial, with the 9 combinations represented by the open circles. The four symbol codes for these combinations indicate the upper (+), lower (–), or central (/) level of factors, as indicated in Table 2.

Table 2
Factor levels in the central-composite factorial design

	Full factorial (2^4 combinations)		Star factorial ($2 \times 4 + 1$ combinations)		
	Lower level (–)	Upper level (+)	Lower level (–)	Center level (/)	Upper level (+)
Factor 1: He step 4 temperature	550°C	850°C	500°C	700°C	900°C
Factor 2: He step 4 duration	1.5 min	4.5 min	1 min	3 min	5 min
Durations of steps 1–3 scaled proportionately					
Step 3	1.33 min	3.7 min	1 min	2.5 min	4 min
Step 2	1.17 min	2.8 min	1 min	2 min	3 min
Step 1	1 min	2 min	1 min	1.5 min	2 min
Factor 3: He steps 1–3 temperatures					
Step 1	125°C	250°C	100°C	187.5°C	325°C
Step 2	267°C if step 4 = 550°C 366°C if step 4 = 850°C	350°C if step 4 = 550°C 450°C if step 4 = 850°C	300°C	292°C if step 4 = 500°C 358°C if step 4 = 700°C 425°C if step 4 = 900°C	450°C
Step 3	408°C if step 4 = 550°C 608°C if step 4 = 850°C	450°C if step 4 = 550°C 650°C if step 4 = 850°C	500°C	396°C if step 4 = 500°C 529°C if step 4 = 700°C 662°C if step 4 = 900°C	575°C
Factor 4: duration of 1 st O ₂ -He step	1 min at 550°C	3 min at 550°C	0.5 min at 550°C	2 min at 550°C	3.5 min at 550°C

set at a particular level. For example, as we show in Table 2, when the step 1 was 125°C and step 4 was 550°C, steps 2 and 3 were 267°C and 408°C, respectively. When the step 1 was at 125°C and the step 4 was 850°C, steps 2 and 3 were 366°C and 608°C. Adjusting steps 1–3 as a group in this way was necessary to make all He step temperatures proportionately placed in the desorption protocol as they are in the NIOSH and IMPROVE protocols and, thus, as TOA might typically be run.

Factor 4. The fourth factor involved the first desorption step in the O₂-He phase where char and native EC are expected to oxidize. We surmised that thermal desorption in O₂ could affect EC/TC accuracy if oxidation of char was perhaps too gentle or too harsh initially, particularly as the laser signal reaches the split point. It is plausible that effects to the surface char particles brought on by harsh oxidation as opposed to gentle oxidation could alter particle refraction, in turn affect char (or native EC) absorptivity, and thus affect laser behavior close to the split point. For the temperature of the first O₂-He step, we chose a value that was consistent with the lower level of factor 1: 550°C for the full factor or 500°C for the star factorial. This is also consistent with the IMPROVE protocol where the first O₂-He step has the same temperature as He step 4 (550°C). Since the temperature of the first O₂-He step was more or less a constant in the factorial design, we varied the duration. The two levels for the full factorial were 1 min and 3 min. The three levels selected for the star factorial were 0.5 min (duration from the NIOSH protocol), 2 min, and 3.5 min.

Measured Responses and Modeled Surfaces

For each sample type, three response variables were measured and modeled. The FID signal was used to determine EC/TC. To track OC charring and potential losses of EC, the maximum laser attenuation (L_{\max}) in the He phase and laser attenuation at the end of the He phase (L_{He4}) were calculated as follows:

$$L_{\max} = \frac{Tr_{\text{init}} - Tr_{\min}}{Tr_{\text{init}}}, \quad [1]$$

$$L_{\text{He4}} = \frac{Tr_{\text{init}} - Tr_{\text{He4}}}{Tr_{\text{init}}} \quad [2]$$

The attenuated laser signal from light passing through the filter was first smoothed with a 13-point quadratic Savitzky-Golay filter (Savitzky and Golay 1964). Tr_{init} is the 10-point average of the smoothed laser signal during the 10 s prior to the start of thermal desorption. Tr_{\min} and Tr_{He4} are, respectively, the minimum smoothed laser signal in the He phase and the smoothed laser signal at the end of He step 4. Both Tr_{\min} and Tr_{He4} are 3-point averages. Spurious variation in the laser signal due to extremes in oven heat, albeit minor, was corrected by fitting a 2nd order polynomial to laser signal versus temperature for pre-cleaned blank quartz-fiber filters and then adjusting the laser signal for each analysis by the offset from the polynomial function.

The L_{\max} response variable was used to assess the positive EC bias that might occur if nonvolatile uncharred OC were measured as native EC during the O₂-He phase. The L_{He4} response variable

was used to assess the extent that native EC might have been unaccountably lost through adventitious oxidation during the He phase, causing a negative EC bias.

Response surfaces of the EC/TC, L_{\max} , and L_{He4} response variables were calculated by fitting a 2nd order polynomial model to measurement data from the complete central-composite factorial design (full plus star factorials) using Matlab software. The model contained 15 terms as shown below: five terms quantified the first-order behavior of each factor (i.e., main effects), four terms quantified within-factor nonlinear behavior (i.e., self-interactions), and six terms quantified factor covariance (i.e., between-factor interactions):

$$\begin{aligned}
 y = & b_0 + b_1x_1 + b_2x_2 && \text{Main effects,} \\
 & + b_3x_3 + b_4x_4 + \dots \\
 & b_5x_1^2 + b_6x_2^2 + b_7x_3^2 + b_8x_4^2 + \dots && \text{Self-interactions,} \quad [3] \\
 & b_9x_1x_2 + b_{10}x_1x_3 + b_{11}x_1x_4 && \text{Between-factor} \\
 & + b_{12}x_2x_3 + b_{13}x_2x_4 + b_{14}x_3x_4 && \text{interactions.}
 \end{aligned}$$

The polynomial model parameters (b) are calculated as follows (Massart et al. 1988):

$$b = (X'X)^{-1}(X'y), \quad [4]$$

where X is a 25×15 matrix with coefficients associated with the model parameters. The first column in X contains ones associated with b_0 . The remaining columns of X contain coefficients corresponding to factor levels from the central-composite design (cols. 2–5), their squares (cols. 6–9), and their cross products (cols. 10–15) for each of the 25 combinations (hence, 25 rows). y is a 25-element column vector for each sample containing the average of measured EC/TC, L_{\max} , or L_{He4} values for each of the 25 combinations. b is the resulting 15-element column vector of model parameters, and elements b_1 to b_{14} should be interpreted as partial derivatives.

Thermal desorption conditions that optimized charring in He and minimized its loss in He were determined from observed relationships among the EC/TC response surfaces and laser attenuation surfaces, L_{\max} and L_{He4} . Optimal conditions were revealed from the intersection of the laser attenuation surfaces when L_{\max} and L_{He4} were equivalent and, therefore, when charring was maximal in the He phase, but loss of char at the end of the He phase was minimal.

RESULTS

EC/TC Measurements

Figures 3 and 4 show the extent to which EC/TC values vary in the full factorial and the star factorial, respectively, for the three sample types. The obvious feature here is the effect on EC/TC from variation in the He step 4 temperature (factor 1). Raising the temperature from 550°C to 850°C caused EC/TC to decrease on average from 0.40 to 0.18 for the lab air particles and 0.52 to 0.26 for the urban PM sample, corresponding to relative

decreases of 55% and 49%, respectively. The EC/TC decrease for the smoldering fire emissions sample was less noticeable yet still substantial (25%). EC/TC decreased to a greater extent when the step 4 temperature was raised from 500°C to 900°C in the star factorial (Figure 4), particularly with lab air particles (70%) and smoldering fire emissions (56%).

As expected, the next largest effect displayed in Figures 3 and 4 is from the step duration in He (factor 2). From the data in Figure 3 for the higher He step 4 temperature (850°C), EC/TC values for the lab air particles, for example, averaged 0.20 when step 4 lasted 1.5 min ((+ - - -), (+ - - +), (+ - + -), (+ - + +)), but 0.16 when step 4 lasted 4.5 min ((+ + - -), (+ + - +), (+ + + -), (+ + + +)); a 20% decrease. Increased step duration did not, however, appear to cause a decrease in EC/TC when the step 4 temperature was 550°C. Furthermore, there is no noticeable effect from factor 2 on the smoldering fire emissions sample, regardless of the step 4 temperature.

Analyses of Variance

Table 3 shows an ANOVA on EC/TC from the full factorial experiment for the lab air sample. Factors 1–3 are statistically significant in the design at the 5% significance level ($F/F_{\text{crit}} \leq 0.05$). Factor 4 does not show significance in this analysis; however, the interaction of factor 1 with factor 4 is significant, as is the interaction of factor 1 with factor 2.

In Table 3, factor 2 accounts for a very small portion of the variance in the factorial design (0.5%) compared to factor 1 (98%). However, if we perform an ANOVA on the two factor 1 levels separately (Table 4), factor 2 has much more statistical significance, but only for the higher factor 1 level. When the He step 4 temperature is 850°C, step duration accounts for 66% of the variance. In contrast, when the He step 4 temperature is 550°C, the duration accounts for only 4% of the variance and the factor is not statistically significant at the 5% significance level. Thus, we see that the ANOVA of the full factorial experiment (Table 3) revealed a significant factor 1 versus factor 2 interaction because He step duration is important only at higher He step 4 temperatures.

In addition to the importance of the He step duration, the importance of the O₂-He step 1 duration (factor 4), becomes clear from the second ANOVA. As shown in Table 4, the O₂-He step duration is significant regardless of whether the temperature of step 4 in He is 550°C or 850°C. However, the amount of variance attributed to factor 4 varies widely between the two He step 4 temperature levels, hence the reason for the factor 1 versus factor 4 interaction shown in Table 3. At 550°C for step 4 in He, duration of the first O₂-He step accounts for 60% of the variance. At 850°C for step 4 in He, the first O₂-He step accounts for 15% of the variance.

The EC/TC Response Surface

EC/TC responses from the factorial design among the three samples shown in Figures 3 and 4 exhibit similar patterns. Therefore, we would expect their response surfaces to be similar.

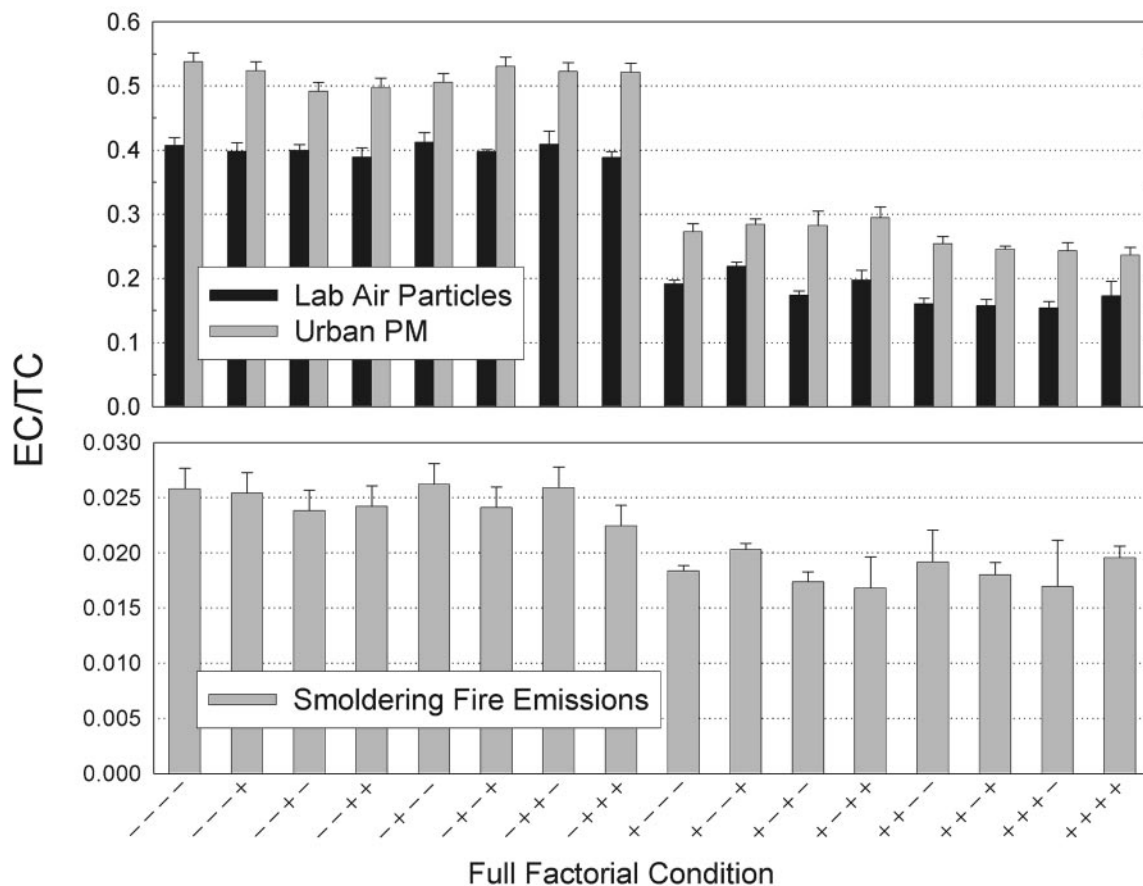


Figure 3. Average EC/TC values of lab air particles, urban PM, and smoldering fire emissions for each combination of thermal desorption parameters in the full factorial design. The four-symbol codes, read from left to right, correspond to those in Figure 2. Error bars indicate standard deviation.

Figure 5 displays the EC/TC response surface for each sample as a function of the He step 4 temperature and duration. Parameters for the 2nd order polynomial model used for each sample are shown in Table 5. The major feature in Figure 5 is the linear (first order or slightly second order) decrease in EC/TC with temperature. As we discuss below, the behavior of the EC/TC response surface with respect to the He-step 4 temperature contrasts substantially with the behavior of the L_{\max} and L_{He4} response surfaces.

Another distinctive feature of the EC/TC response surfaces is the curvature along the step duration axis. For both the lab air particles and urban PM, the surfaces show an asymptotic decrease in EC/TC as step duration increases. The smoldering fire emissions sample does not exhibit this effect. As noted in the above section “Analysis of Variance”, the statistical significance of the effect of He step duration on EC/TC is unequivocal.

We do not show uncertainties in the EC/TC response surfaces in Figure 5; however, their magnitudes are noteworthy in that they are remarkably consistent and small for the lab air sample and urban PM. For lab air particles, the pooled standard devi-

ation relative to the average EC/TC value for all 25 factorial combinations is 4.5%. The standard uncertainty (the NIST/ISO analog to the confidence interval at 5% significance (ISO 1993; Taylor and Kuyatt 1994)) for the lab air EC/TC surface is 0.8%, based on $n = 112$, a coverage factor of 2 (analogous to Student’s t), and relative to the average EC/TC values in the factorial design. For the urban PM sample, the pooled standard deviation relative to the EC/TC average is 5.4%, and the standard uncertainty relative to the EC/TC average is 1.7%, based on $n = 39$. For the smoldering fire emissions sample, the pooled standard deviation relative to the EC/TC average is 14%, and the relative standard uncertainty is 5.2%, based on $n = 30$. Thus, the relative standard uncertainty for the smoldering fire emissions sample is at least 3 times higher than for the other two samples. For each sample, uncertainties are derived from the pooled variance of all replicated factor combinations.

Measurements from the Attenuated Laser Signal

Figure 6 shows a series of laser responses with temperature profiles (solid line) from thermograms for selected full factorial

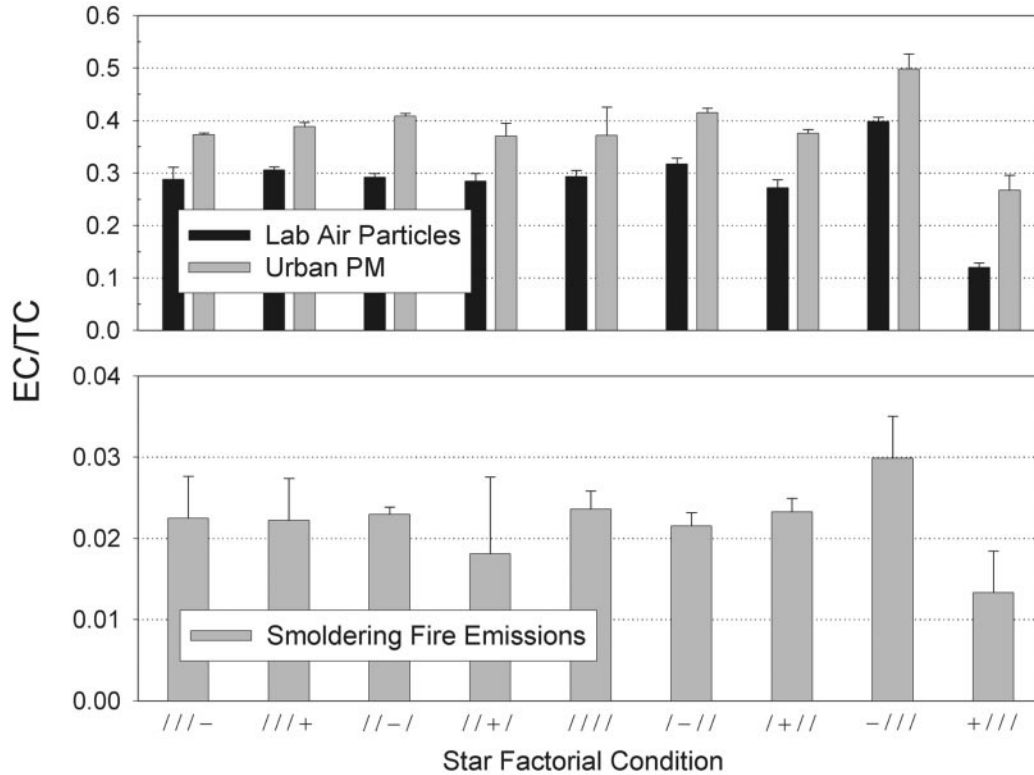


Figure 4. Average EC/TC values of the three sample types for each combination of thermal-desorption temperature and time parameters in the partial (star) factorial design. The four-symbol codes correspond to those in Figure 2. Error bars indicate standard deviation.

conditions. The initial attenuated laser signals (i.e., at 0 s) are offset because the initial transmission of light through the filter is due to varying total light-attenuating masses. For all conditions except those in Figure 6a (---), where step durations and temperatures are at their lower levels, the smoldering fire emissions charred in He to a much greater extent than lab air particles or urban PM. Nevertheless, all three samples charred to a greater extent when step 4 in He was 850°C than when the temperature was 550°C.

A surprising observation is that in the (---) case charring of the smoldering fire emissions continues into the O₂-He phase. In fact, most of the charring of this material occurs there. Clearly, for the other three factorial conditions shown in Figure 6 where the He step 4 temperature is 850°C, no further charring takes place in the O₂-He phase. Furthermore, we observed that no further charring took place in the O₂-He phase for the smoldering fire emissions sample when the He step 4 temperature was 700°C.

Laser responses for the three samples also behave differently for the three factorial conditions with step 4 in He at 850°C (Figures 6b–d). For lab air particles and urban PM, the attenuated laser signal clearly reaches a minimum and then rises during the

lengthy step 4 heating, i.e., conditions (+ + --) and (+ + +-). This is clear evidence that there is either loss of char from the filter in the He phase, a loss of native EC, or a decrease in the absorptivity of either under these conditions. In fact, in Figure 6d the laser signal rises slightly during step 3 in He (650°C) for the lab air particles and urban PM. There is no evidence, however, of the loss material or decrease in absorptivity in the He phase for smoldering fire emissions.

As explained in the above section “Measured Responses and Modeled Surfaces,” L_{\max} and L_{He4} , were calculated from the attenuated laser signal to assess charring during the He phase. We now explore the relationship between the EC/TC measurements and laser attenuation. In Figure 7, we show L_{\max} (filled circles) and its L_{He4} counterpart (open circles) with respect to EC/TC for lab air particles, urban PM, and smoldering fire emissions. For lab air particles and urban PM (Figures 7a and b), the points fall within three general clusters along the EC/TC axis. For example, in Figure 7a the clusters are centered near 0.16, 0.29, and 0.40 along the EC/TC axis. For the most part, the clusters correspond to the factorial conditions associated with the three levels of the He step 4 temperature in the factorial design. With an exception labeled (+///), points in the first cluster along the EC/TC axis

Table 3
Analysis of variance¹ on EC/TC of lab air particles from the full factorial experiment

Source	DF ²	Sum of squares	Mean squares	F-value	F/F_{crit} ³	Fraction of total variance ⁴
Blocks	3	2.27E-06	7.56E-07	0.00451	>0.999	9.38E-07
F1	1	0.789	0.789	4710	3.46E-47	0.979
F2	1	0.00374	0.00374	22.3	2.31E-05	0.00464
F3	1	0.000876	0.000876	5.23	0.0270	0.00109
F4	1	3.61E-05	3.61E-05	0.215	0.645	4.48E-05
F1.F2	1	0.00563	0.00563	33.6	6.30E-07	0.00698
F1.F3	1	2.74E-07	2.74E-07	0.00164	0.968	3.40E-07
F1.F4	1	0.003667	0.00367	21.9	2.67E-05	0.00455
F2.F3	1	0.000677	0.000677	4.04	0.0505	0.000810
F2.F4	1	0.000669	0.000669	3.99	0.0518	0.000830
F3.F4	1	2.80E-05	2.80E-05	0.167	0.685	3.48E-05
Residual	45	0.00754	0.000168			0.000208
Total	63	0.813				

¹ANOVA encompassed two- to four-way factor interactions; however, only two-way interactions are shown in the table. No three- or four-way interactions were significant at the 5% significance level.

²Degrees of freedom.

³Factor or factor interaction is significant when F/F_{crit} is ≤ 0.0500 .

⁴Ratio of mean squares for an individual factor, factor interaction, or the residual to the total of mean squares for all entries including three- and four-way interactions.

are associated with the 850°C He step 4 level of the full factorial. The middle cluster is associated with the 700°C level from the star factorial. With an exception labeled (-///), the third cluster is associated with the 550°C He step 4 full-factorial level. The exceptions are associated with the star factorial condition with the He step 4 temperature at 900°C (+///) and 500°C (-///).

Figures 7a and b clearly show that EC/TC increases as L_{max} decreases. While the results for smoldering fire emissions (Figure 7c) do not reveal distinctive clusters along the EC/TC axis, the same trend exists. Thus, as the He step 4 temperature increases, EC/TC decreases and laser attenuation from charring (L_{max}) increases. In addition, Figures 7a and b reveal that the

Table 4
Analyses of variance¹ on EC/TC of lab air particles from the full factorial experiments separated into the two levels of the He step 4 temperature (factor 1)

Source	DF ²	He step 4 temperature at 550°C			He step 4 temperature at 850°C		
		F-value	F/F_{crit} ³	Fraction of total variance ⁴	F-value	F/F_{crit} ³	Fraction of total variance ⁴
Blocks	3	0.535	0.663	0.0392	0.490	0.693	0.00522
F2	1	0.532	0.474	0.0390	60.4	1.31E-07	0.643
F3	1	2.33	0.142	0.171	2.96	0.100	0.0315
F4	1	8.21	0.00925	0.601	14.4	0.00105	0.154
F2.F3	1	0.0639	0.803	0.00468	7.26	0.0136	0.0774
F2.F4	1	0.768	0.391	0.0562	4.00	0.0586	0.0426
F3.F4	1	0.161	0.693	0.0118	1.08	0.310	0.0115
Residual	21			0.0732			0.0107
Total	31						

¹ANOVA encompassed two- and three-way factor interactions; however, only two-way interactions are shown. The three-way interaction (F2.F3.F4) was not significant at the 5% significance level.

²Degrees of freedom.

³The factor or factor interaction is significant when F/F_{crit} is ≤ 0.0500 .

⁴Ratio of mean squares for an individual factor, factor interaction, or the residual to the total mean squares for all entries, including the three-way interaction.

Table 5

Parameters from 2nd order polynomial models (Equation (3)) used to calculate EC/TC surfaces

	Lab air particles	Urban PM	Smoldering fire emissions
b_0	6.31E-01	8.60E-01	2.96E-02
b_1	4.32E-05	-5.90E-04	3.56E-06
b_2	2.38E-04	2.03E-02	-1.44E-05
b_3	-3.95E-04	-3.27E-04	3.66E-05
b_4	-5.63E-02	1.48E-02	-1.44E-03
b_5	-5.36E-07	-3.55E-08	-2.62E-08
b_6	3.42E-03	2.77E-03	-5.84E-05
b_7	5.69E-07	1.77E-07	-1.58E-07
b_8	6.83E-03	-1.51E-03	-1.51E-04
b_9	-4.17E-05	-6.11E-05	3.91E-07
b_{10}	-5.95E-09	2.65E-07	-4.11E-10
b_{11}	5.05E-05	-3.83E-06	3.50E-06
b_{12}	3.45E-05	8.93E-06	3.40E-06
b_{13}	-2.15E-03	-3.71E-04	-2.30E-04
b_{14}	1.07E-05	-1.35E-05	6.94E-07

L_{\max} and L_{He4} points behave differently in each cluster for these samples. In the third cluster along the EC/TC axis, L_{\max} and L_{He4} points coincide. However, they diverge in the second cluster and then to a greater extent in the first cluster. Overall, the smoldering fire emissions behave differently in that there is virtually no divergence between L_{\max} and L_{He4} points in Figure 7c.

In general, Figures 7a and b show that the extent to which L_{He4} and L_{\max} diverge is clearly related to the step 4 temperature in He and the EC/TC ratio. However, we can further separate the first cluster of Figure 7a into two groups, delineated by ellipses a_1 and a_2 . Group a_1 has eight points that exhibit the highest laser attenuation of all factorial combinations and the L_{\max} and L_{He4} points coincide, unlike those in a_2 . Points in a_1 exhibit the most charring as indicated by relatively large L_{\max} values. In addition, there is minimal loss of pyrolysis OC, native EC, or change in the absorptivity in the He phase as indicated by the relatively large L_{He4} values and the coinciding of L_{He4} and L_{\max} values. Conditions that are common to group a_1 are 850°C in He for 1.5 min. In contrast, conditions that are common to group a_2 are 850°C in He for 4.5 min. (Each of the L_{He4} points in a_2 corresponds to an L_{\max} point directly above). EC/TC values in a_1 are higher on average than those in a_2 . It is important to note that if the divergence of L_{\max} and L_{He4} were due to a decrease in absorptivity rather than a loss of char or native EC, we would not expect to see a corresponding decrease in EC/TC. Conditions represented by group a_1 are the optimal conditions in the factorial design for the indoor air sample, based on the laser signal, compared to those for group a_2 because while EC/TC values are higher in a_1 , charring is also optimal in the He phase.

The same relationships between EC/TC and both L_{\max} and L_{He4} exist for urban PM, shown in Figure 7b. The first cluster along the EC/TC axis is for the most part associated with step 4 at 850°C in He and can be further separated into two

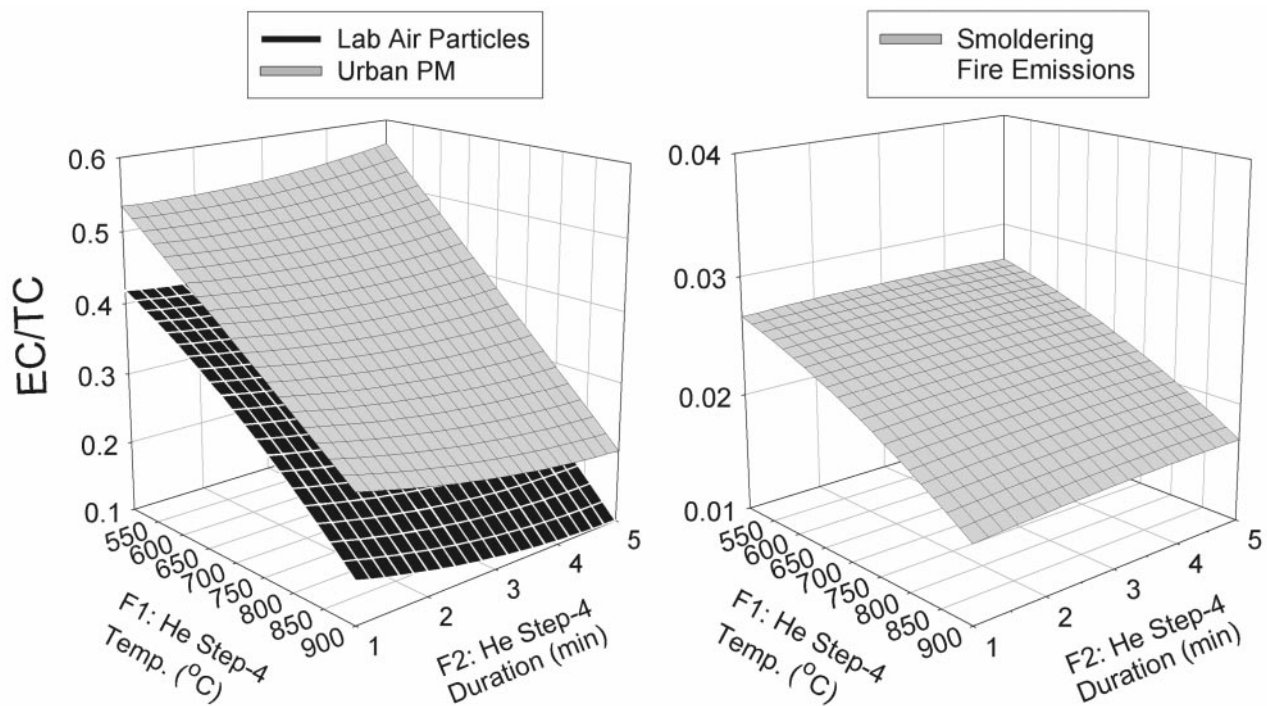


Figure 5. EC/TC response for lab air particles, urban PM, and smoldering fire emissions as surfaces with respect to the He step 4 temperature (factor 1) and the He step 4 duration (factor 2).

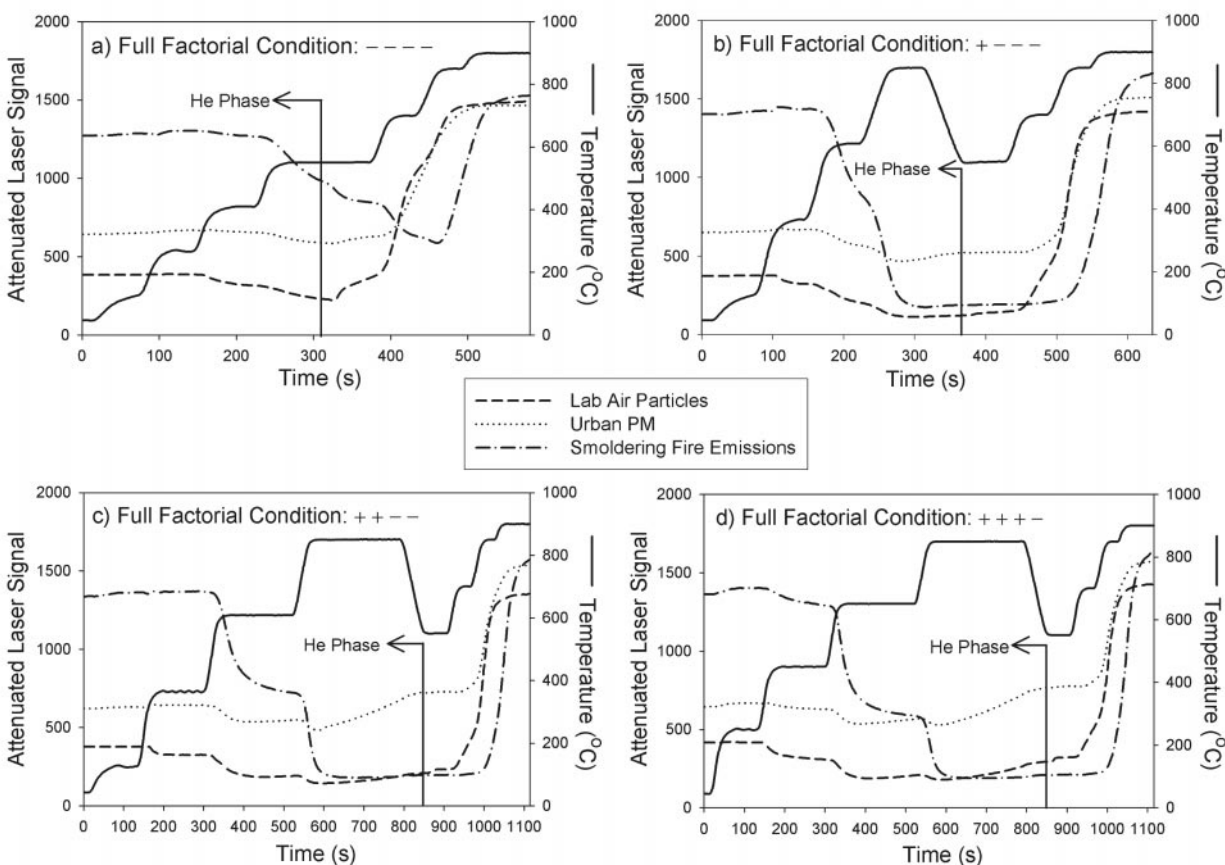


Figure 6. Comparison of laser responses from representative thermograms of four full-factorial conditions: (a) (---), (b) (+---), (c) (++++), and (d) (++++). Included for each factorial condition is the temperature profile.

groups ($b1$, $b2$). (The point labeled (+//)) in the first cluster is associated with the star factorial condition for step 4 at 900°C in He (and its L_{\max} counterpart directly above.) The four L_{\max} points in $b1$ nearly coincide with the corresponding $L_{\text{He}4}$ points, and they have the largest EC/TC values in this cluster. Conditions that are common to group $b1$ are 850°C in He for 1.5 min, as they were to group $a1$ in Figure 7a. Similarly, conditions that are common to group $b2$ are 850°C in He for 4.5 min, as they were to group $a2$ in Figure 7a. Conditions represented by group $b1$ are optimal in the factorial design for the urban PM sample, because charring was optimal in the He phase based on the near alignment of L_{\max} and $L_{\text{He}4}$. As a result of optimal charring, EC/TC values in group $b1$ are higher than those in $b2$.

SEM Images

In addition to determining EC/TC ratios and laser attenuation for the various conditions in the factorial design, we observed the effect of varying He-phase conditions on individual particles with scanning electron microscopy (FEI-Phillips-Electroskan model 2020 Environmental Scanning Electron Microscope; 20 kV accelerating voltage; chamber pressure 612 Pa (4.6 Torr)

of water vapor; sample placed 2 mm below the gaseous secondary electron detector). In these experiments, filter sections of lab air particles were removed from the instrument immediately after the He phase ended and placed in clean, enclosed Petri dishes prior to SEM imaging.

We selected three factorial conditions for imaging: (1) a full factorial condition representing step 4 at 550°C in He (---), (2) a star factorial condition representing step 4 at 700°C in He (/ - //), and (3) a full factorial condition representing the step 4 at 850°C in He (+---). Representative plots of the laser response for (1) and (3) are shown in Figures 6a and b. Figure 8 shows representative examples of several images of lab air particles taken for these conditions. For each condition, we show a low magnification ($250\times$ or $500\times$) image and a high magnification ($1650\times$ or $2550\times$) image.

From the high magnification images (Figures 8b, d, and f), numerous smaller particles ($<1\ \mu\text{m}$ in diameter) remained on filters following heating at 550°C , 700°C , or 850°C . For the 550°C treatment (Figure 8a) and the 700°C treatment (Figure 8c), variously shaped larger particles ($>2\ \mu\text{m}$ in length) were also present. In contrast, large particles were clearly less abundant from the 850°C treatment, as shown in Figure 8e.

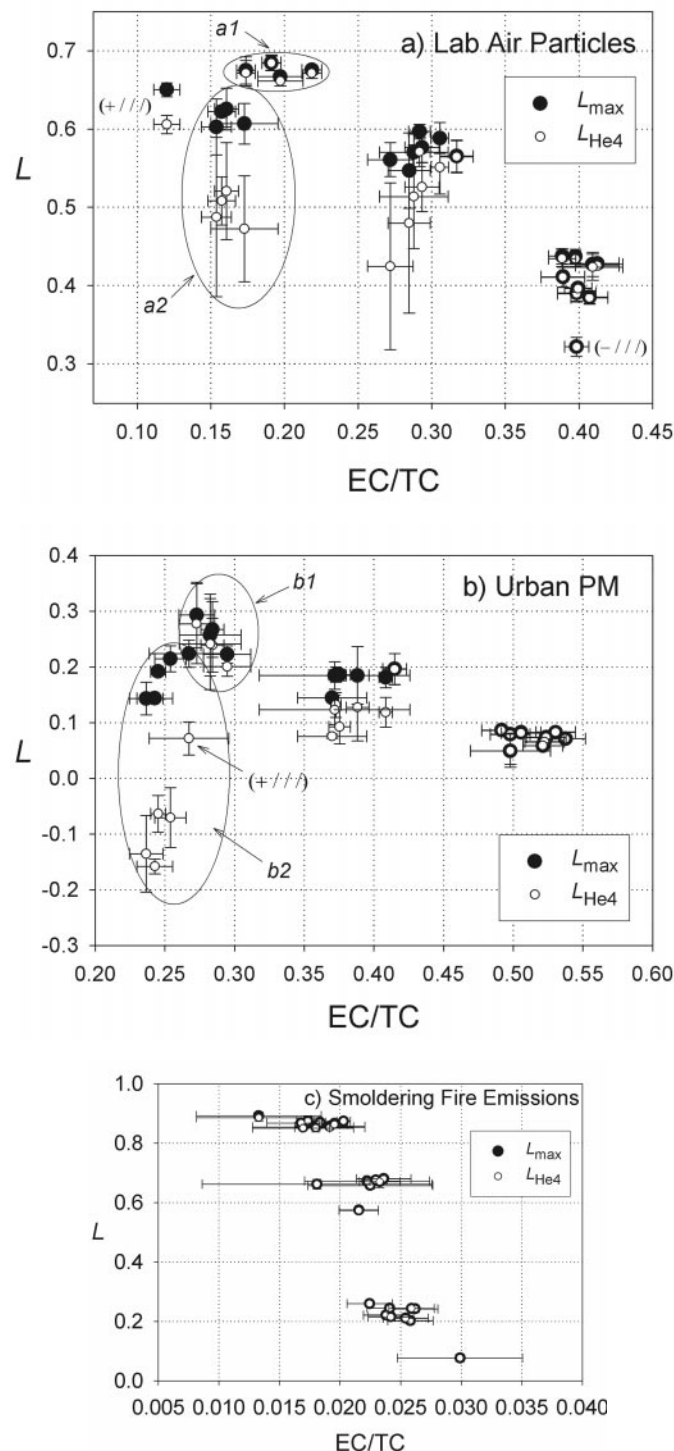


Figure 7. EC/TC versus maximum laser attenuation (L_{max} , closed circles) and versus laser attenuation at the end of He step 4 (L_{He4} , open circles) for the various thermal desorption protocols in the complete factorial design. (a) Lab air particles; (b) urban PM; (c) smoldering fire emissions. Error bars indicate standard deviation. Points labeled (+ ///) and (- ///) are star-factorial “outliers” in that their nearest neighbors are full-factorial points.

It is likely that a high proportion of the particles in the images $<1 \mu\text{m}$ are aggregates of primary ultrafine particles from combustion and have a high EC content. Xiong and Friedlander (2001) have shown that aggregates of urban air particles consist of 10 to 180 primary soot-like particles with diameters of 6 nm to 100 nm. Aggregates $\geq 2 \mu\text{m}$ were not found in their study. For soot from a modern diesel engine, Shi et al. (2000) found that the primary particles ranged from 10 nm to 40 nm. Therefore, the larger particles in Figures 8a and c are likely charred remains of non-agglomerated particles. We would expect these particles to have a relatively low EC content. The presence of these large particles suggests that the 550°C and 700°C treatments for the sample were inadequate to either volatilize the carbon or pyrolyze it in OC-rich particles.

DISCUSSION

The data presented in Figures 6 and 7 clearly indicate that charring increases as the He step 4 temperature increases. Moreover, Figure 7 reveals that there is a direct relationship between the extent of charring in He and EC/TC. Within the He phase, OC is either volatilized or pyrolyzed, and maximal charring from pyrolysis minimizes the likelihood that uncharred OC will be oxidized in the O_2 -He phase and measured as native EC. It is clear from Figure 6 that when charring is maximal for a sample, the laser response must rise further in the O_2 -He phase to reach the initial laser signal at the split point than when charring is minimal. If the laser signal reaches the split point before all OC is charred, any uncharred OC remaining on the filter after the split point would be measured as native EC, causing a positive bias.

In Figure 6 there was evidence that in some cases change in the laser response in the O_2 -He phase might correct for inadequate charring in the He phase. In Figure 6a, the optical density of the smoldering fire sample clearly continued to change in O_2 -He. However, the attenuated laser signal was still only about 60% of the attenuation when the TOA was run at the higher step 4 temperature in He (Figures 6b–d). Thus, the TOA laser response did not correct for all of the uncharred OC from the He phase when step 4 in He was at 550°C (Figure 6a). Therefore, EC/TC is optimized to eliminate the positive bias only when charring is maximized during the He phase as measured by L_{max} .

An unwanted effect from maximizing OC charring at high temperatures is the potential negative bias due to the loss of native EC before the split point is reached. This should not affect EC accuracy if the laser signal accounts for this loss by a proportional rise in the attenuated laser signal. However, the separation of L_{max} and L_{He4} values for lab air particles (Figure 7a) and especially for urban PM (Figure 7b) versus EC/TC suggests that there is a direct relationship between EC/TC and the loss of char in the He phase. EC/TC decreases as loss of char in He increases. If we assume that native EC and instrument-produced char are the result of similar high-temperature processes, the chemical and optical properties of these substances will be similar. Thus,

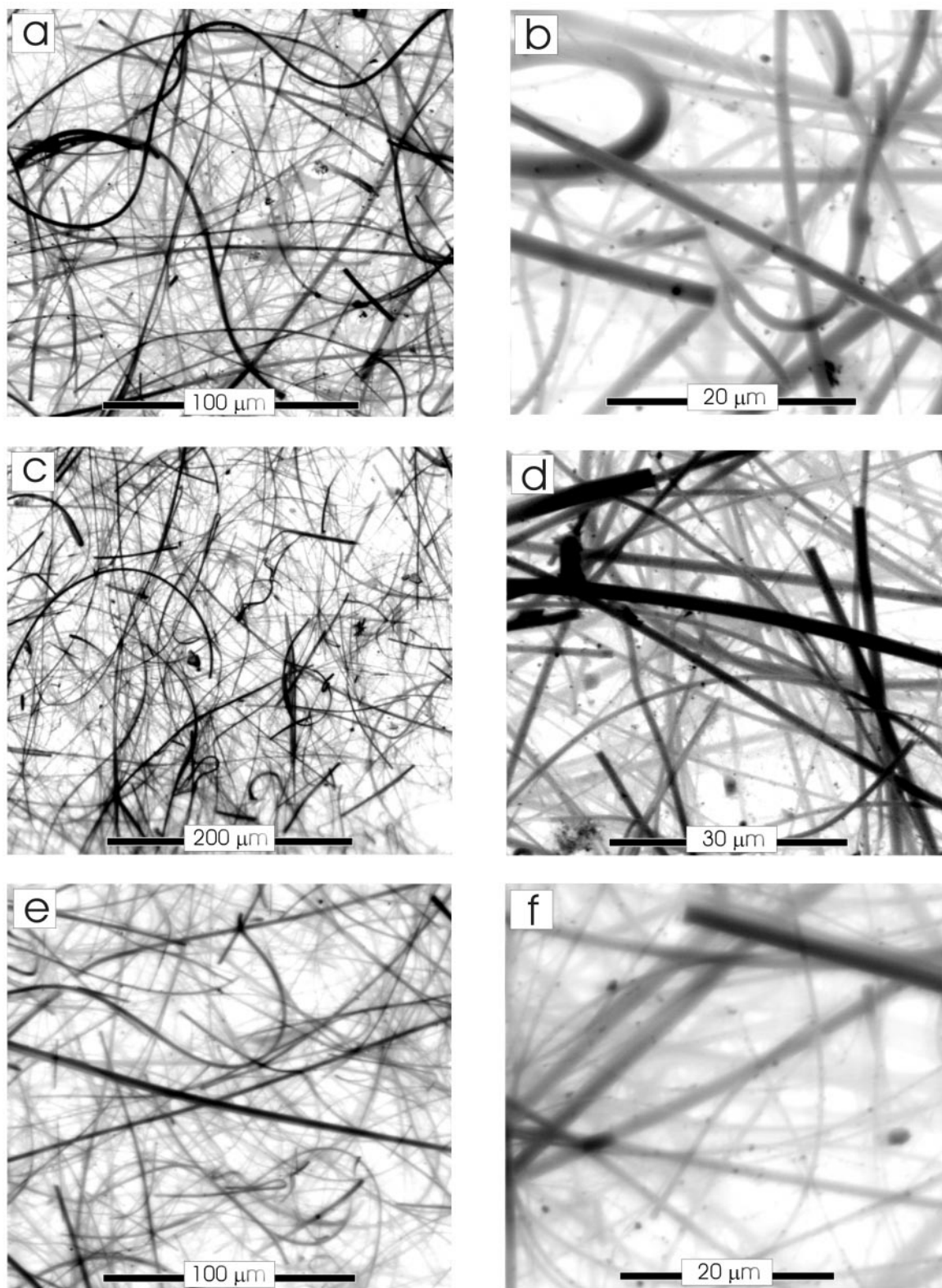


Figure 8. Scanning electron microscope images at both low (a, c, e) and high (b, d, f) magnification of lab air particles on quartz-fiber filters at the end of step 4 in He for two full factorial protocols and one star factorial protocol. For (a) and (b) He step 4 was 550°C based on the (---) protocol, for (c) and (d) He step 4 was 700°C based on the (///) protocol, and for (e) and (f) He step 4 was 850°C based on the (+---) protocol.

the loss of OC char in He can serve as a surrogate for monitoring the negative bias.

As further evidence of the importance of monitoring char as a surrogate for native EC, we note in Figure 7a the two-point “outlier” associated with the He step 4 star factorial condition at 900°C. EC/TC for these points (0.12) is 40% less than the average EC/TC value for group *a1* points (0.20). Clearly, the low EC/TC result in this case indicates a loss of EC at 900°C in He. The importance of this observation is further substantiated by the relatively low uncertainties of the “outlier” with respect to both EC/TC and *L*-values. Again, our results indicate that it is important to maximize char production in He and to minimizing its loss after it is formed.

The reason that the TOA laser signal may not correctly track the loss of EC is perhaps related to changes in the absorptivity of EC during TOA analysis. The absorptivity of native EC subjected to high temperatures (e.g., $\geq 850^\circ\text{C}$) in He may be different from that of native EC oxidized at lower temperatures in O_2 -He due to changes in the particle refractive index. Thus, we cannot assume that the optical behavior of native EC in a high-temperature inert environment is the same as that in a lower-temperature oxidizing environment. The smoldering fire sample in our experiments did exhibit a substantial optical-density change in O_2 -He due to charring, as we indicated in the above section “Measurements from the Attenuated Laser Signal”. However, this occurred to a great extent at lower temperatures (550–700°C in Figure 6a) rather than at higher temperatures, where significant loss of native EC might occur.

In this study, we presume that the high-temperature loss of OC char (and native EC) mainly involves redox reactions with solid-phase compounds in the sample. An example is the high-temperature reaction of Fe_2O_3 with EC involving perhaps the cycling of surface-bound CO and CO_2 ($\text{Fe}_2\text{O}_3 + 3\text{CO} \rightarrow 2\text{Fe} + 3\text{CO}_2$; $\text{CO}_2 + \text{C} \rightarrow 2\text{CO}$). We do not believe that the loss of pyrolytic OC and native EC is merely an instrument artifact caused by O_2 contamination in the He phase. If this were the case, we would expect loss of char in He from the smoldering fire sample, which clearly did not occur.

Step 4 in Helium

Urban PM. If we plot the response surfaces for L_{\max} and L_{He4} in the same dimensional space, the intersection between the response surfaces points to a region where we approach optimal TOA conditions. Beginning with the *L* response surfaces for urban PM, Figure 9 shows two views of the surfaces (L_{\max} -gray and L_{He4} -black) as functions of the He step 4 temperature and duration. Figure 9a shows the entire model surfaces. Figure 9b shows the part of the surface where L_{\max} is largest and where L_{\max} and L_{He4} intersect, i.e., at the distal corner of Figure 9a.

An important characteristic of the L_{\max} surface is its curvature. In Figure 9a, L_{\max} increases with the He step 4 temperature with apparent second-order behavior. For example, when step 4

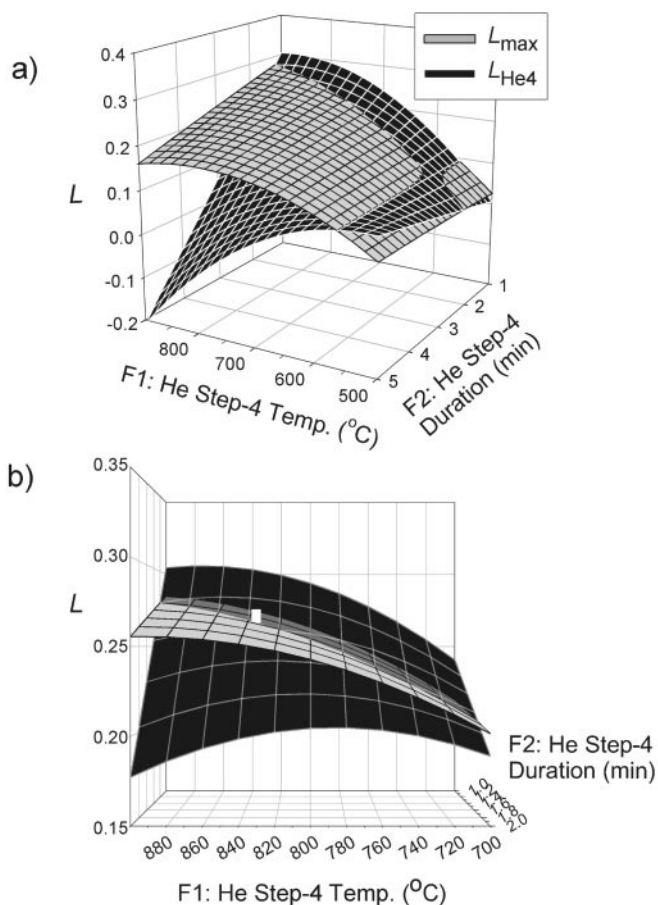


Figure 9. Views of the *L* response surfaces for urban PM sample as functions of the He step 4 temperature and duration. Factor 3 is fixed at the center level for the star factorial (e.g., He step 1 temperature: 188°C). Factor 4 (O_2 -He step 1 duration) is at 2 min. (b) is the magnified view at the distal corner of the overall surface shown in (a). The vertical white bar shown at the surface intersection at 835°C in (b) is the standard uncertainty (0.006) based on a pooled standard deviation from full and star factorial measurements for *L* ($n = 71$, $k = 2$).

lasts 5 min, maximum charring occurs about 800°C. Thus, there is a diminishing benefit from increasing the step 4 temperature in He to maximizing charring.

We now compare the curvature of the L_{\max} surface for urban PM with the lack of curvature in the EC/TC surface (Figure 5). (Note that the temperature and duration axes are reversed from those in Figure 5 to better display the L_{\max} and L_{He4} surfaces.) While the L_{\max} surface levels off around 800°C at 5 min, the EC/TC surface continues to decrease in a first order manner. This comparison provides clear evidence of a loss of native EC at high temperature. If there were no loss of native EC under these conditions, the EC/TC surface would also be second order and resemble the L_{\max} surface. However, if we compare the EC/TC and L_{\max} surfaces at the shortest He step 4 duration (1 min), the

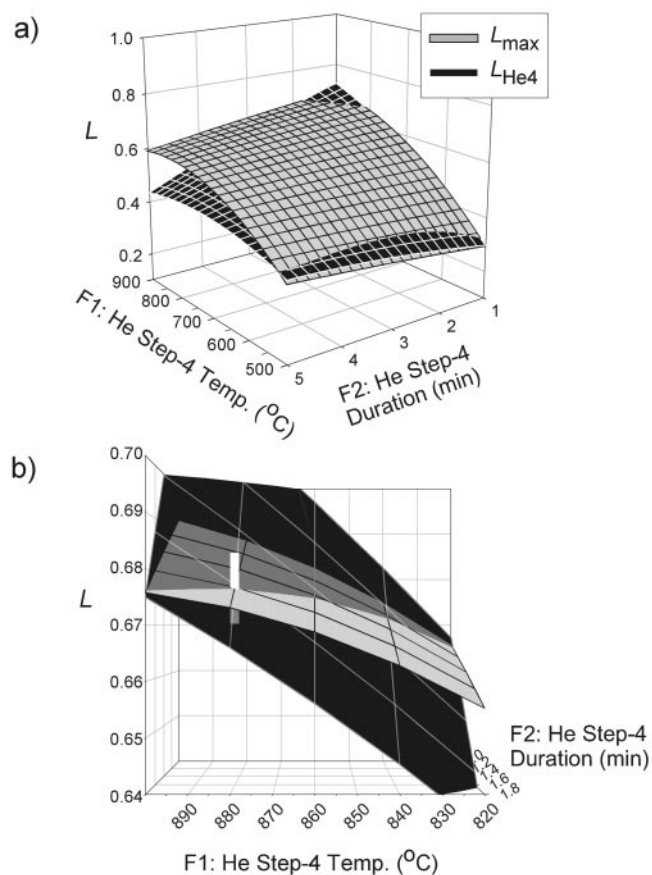


Figure 10. Views of the L response surfaces for the lab air sample as functions of the He step 4 temperature (Factor 1) and duration (Factor 2). Factor 3 is fixed at the center level for the star factorial (e.g., He step 1 temperature: 188°C). Factor 4 (O_2 -He step 1 duration) is at 2 min. (b) Magnified view at the distal corner of the overall surface in (a). The vertical white bar shown at the surface intersection at 880°C in (b) is the standard uncertainty (0.007) based on a pooled standard deviation from all full and star factorial measurements for L ($n = 112$, $k = 2$).

L_{max} surface is more first order-like and begins to resemble the EC/TC surface.

As Figure 9 shows, the L_{max} and L_{He4} surfaces for urban PM differ sharply, particularly at higher He step 4 temperatures, allowing us to clearly view the intersection between the two surfaces. Along the intersection shown in Figure 9b, L_{max} and L_{He4} are equal, and there is no loss of char during step 4 at those conditions. The optimal region begins at the intersection between the two surfaces and includes the area of the L_{max} surface beneath the L_{He4} surface. In this analysis, a high step 4 temperature (e.g., 900°C) should be accompanied by a short step 4 duration (e.g., 1 min); a lower step 4 temperature (e.g., 700°C) should be accompanied by a longer step 4 duration (e.g., 1.7 min). As noted in the above section “SEM Images,” SEM images (Figure 8) reveal that a lower step 4 temperature such as 700°C does not

produce a qualitative change in the large OC-rich lab air particles, suggesting that pyrolysis at 700°C is inadequate for that sample. Conversely, the disadvantage to using a higher temperature such as 900°C is the likely loss of native EC in the He phase as evidenced by the differences between the EC/TC and the L_{max} surfaces. Thus, native EC loss can occur at high temperatures as OC charring increases. Moreover, because we use loss of char as a surrogate for native EC loss, the L_{He4} surface may not fully exhibit this loss.

Laboratory Air Particles. Figure 10 shows the L_{max} and L_{He4} surfaces for the lab air sample as functions of the He step 4 temperature and duration. Distinctive similarities exist between the lab air particles and urban PM for the L_{max} surface. Curvature in the L_{max} surface is clearly evident in Figure 10a over the range of step durations, so the benefit from increasing the step temperature diminishes as temperature and duration increase. Again, we compare this curvature with the lack of it in the corresponding EC/TC surface at high temperatures (Figure 5). We conclude that EC loss occurs as charring continues at high temperatures, particularly when step duration is lengthy. Moreover, the L_{max} surface for lab air particles begins to resemble the corresponding EC/TC surface as step duration becomes smaller.

Smoldering Fire Emissions. For the smoldering fire sample, L_{max} and L_{He4} surfaces are nearly identical (Figure 11). Curvature in the L_{max} surface is quite evident, however, and contrasts sharply with the lack of curvature in the corresponding EC/TC surface (Figure 5). Thus, the loss of native EC may occur at high He temperatures for this sample. If so, the use of L_{He4} to gauge the loss of native EC does not work in this case.

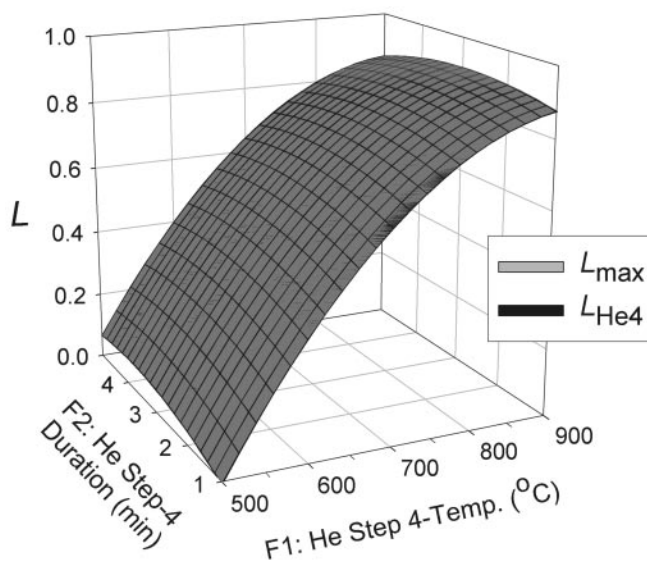


Figure 11. L response surfaces for the smoldering fire emissions sample as functions of the He step 4 temperature and duration. Factor 3 is fixed at the center level of the star factorial (e.g., He step 1 temperature: 188°C). Factor 4 (O_2 -He step 1 duration) is at 2 min.

Generalized Optima for Temperature and Duration of Step 4 in Helium To converge on the optimum temperature and duration for step 4 in He for our samples, we look for common features between the surfaces for urban PM and lab air particles near the surface intersections in Figures 9b and 10b. Results from the smoldering fire emissions do not provide insight for optimizing step 4 because no sufficient intersection in the L_{\max} and L_{He4} surfaces exists (Figure 11).

For the lab air particles (Figure 10b), the L maximum along the intersection occurs around 880°C and 1.6 min. Thus, there is clearly no advantage to increasing the temperature beyond 880°C for this sample. For the urban PM, there does appear to be an advantage to increasing the temperature beyond this point (Figure 9b) as long as the step duration is short. However, loss of native EC is still an important consideration. Thus, there is no advantage to increasing the He step 4 temperature beyond 880°C for either the lab air sample or urban PM. Our selection of an optimum He step 4 temperature is based on the standard uncertainty in L at 880°C for the lab air sample (vertical bar in Figure 10b). If we select the lower limit of the uncertainty interval (0.670) and project this L value along the L_{\max} - L_{He4} intersection, we find a temperature of 835°C and duration of 1.2 min. Thus, 835°C for 72 s is the optimal instrument settings for step 4 in He for ambient air samples from this study. There is no evidence to suggest that these settings are not applicable for the smoldering fire emissions because, from Figure 11, there is no clear benefit to extending the He step 4 temperature beyond 835°C.

Carbonate is generally not problematic at 835°C, since it usually appears as a narrow peak between 700°C and 800°C, indicating the need to either remove the thermogram carbonate peak from the raw data or remove carbonate chemically from the sample by HCl vapor and then reanalyze. CaCO₃ spiked to our lab air sample showed the carbonate carbon peak appearing around 750°C to 800°C.

Optimizing Steps 1–3 in Helium

Figures 12 and 13 shows the L response surfaces for the urban PM and lab air samples, respectively, as a function of the He step 4 temperature and the temperatures of steps 1–3 in He as they were varied in concert as factor 3. For these surfaces, the He step 4 temperature is 850°C and the O₂-He step 1 duration is 2 min.

Among steps 1–3 in He, we would expect the greatest effect from step 3 because most charring occurs at this temperature. Also, as we see in Figure 6d, the step 3 temperature can be high enough to cause loss of char if the step is lengthy. However, the ANOVA (Table 4) on lab air particles indicated that varying the temperatures of steps 1–3 did not result in a significant change in EC/TC when step 4 in He was at 850°C.

In Figure 12, we focus on the surface intersection when the He step 3 temperature ranges from 600°C to 667°C, which occurs when He step 4 is <2 min. Clearly, L_{\max} increases, hence overall

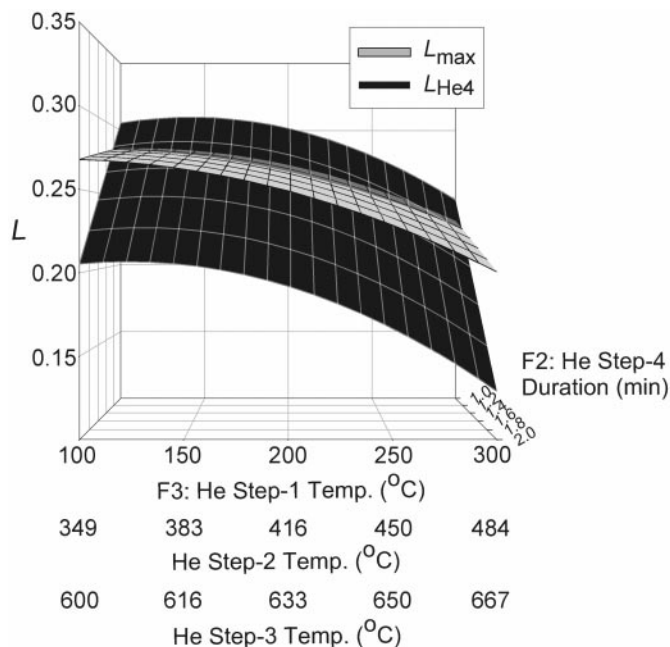


Figure 12. L response surfaces for the urban PM sample as functions of the temperatures of steps 1–3 in He and the He step 4 duration. The He step 4 temperature is at 850°C, and the O₂-He step 1 duration (Factor 4) is at 2 min.

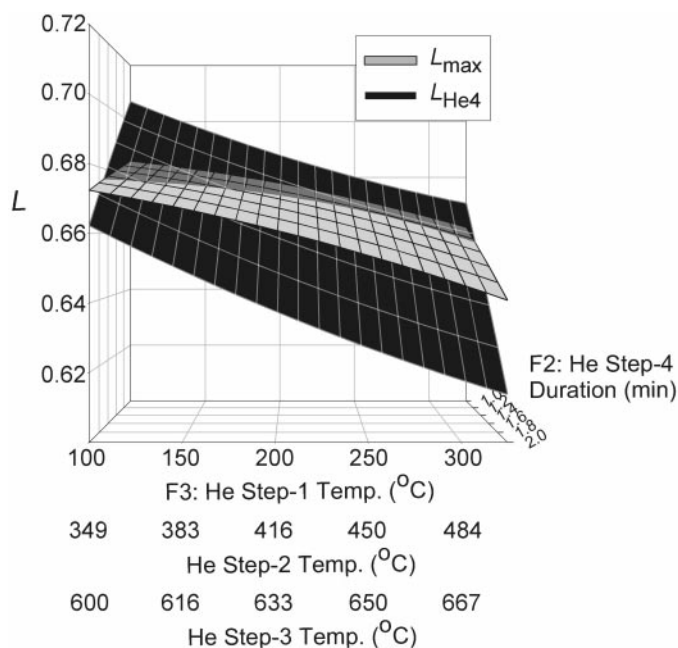


Figure 13. L response surfaces for the lab air sample as functions of the temperatures of steps 1–3 in He and the He step 4 duration. The He step 4 temperature is at 850°C, and the O₂-He step 1 duration (Factor 4) is at 2 min.

charring increases, as the temperature of step 3 decreases, and as steps 1 and 2 decrease by design. In Figure 13, the optimal intersection of L_{\max} and L_{He4} occurs when step 3 is between 600°C and approximately 630°C. While we have not proven statistically that higher step 3 temperatures cause a loss of native EC, there is clearly no advantage to raising this temperature. From results shown in Figures 12 and 13, it is prudent to limit the step 3 temperature, as well as the temperatures of steps 1 and 2. We concluded that the optimal temperatures of steps 3 and 2 in He are at the lower level of the full factorial design (Table 2)—that is, 608°C and 366°C, respectively. For the smoldering fire sample, no effect on the L_{\max} surface was observed from a change in factor 3. Thus, the same step temperatures are appropriate for this sample.

We note that when the lower step 1 temperature from the full factorial was used (125°C) no OC desorbed from either the urban PM or lab air particles at this temperature. Thus, such a low temperature served no purpose. Desorbed OC first appeared in our factorial experiment when the He-step 1 temperature was 188°C. We conclude, therefore, that an appropriate step 1 temperature for both the ambient air samples and the source emissions sample is 188°C.

Optimizing Step 1 in the O₂-He Phase

The L response surfaces do not provide a means to optimize the duration of the first step in O₂-He. Here, we must rely solely on the EC/TC response surface. As mentioned in the above section “Analysis of Variance,” the ANOVA (Table 4) on lab air particles indicated that factor 4 accounts for a significant portion of the variance in the full factorial when the step 4 temperature

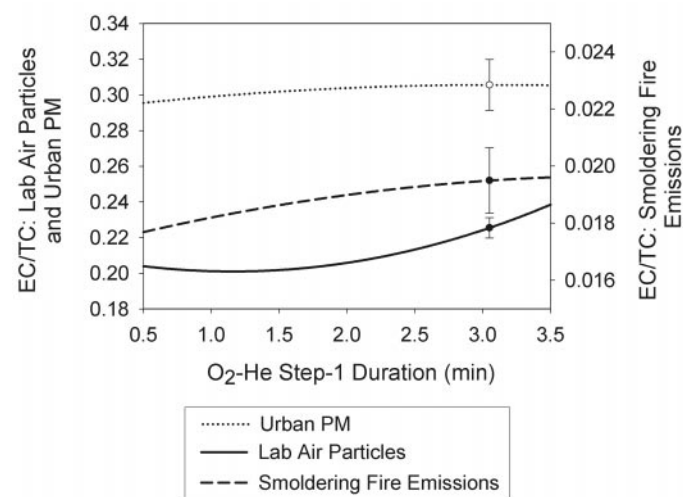


Figure 14. Change in EC/TC from the response surface as a function of the O₂-He step 1 duration. The He step 4 temperature and duration are 840°C and 1.5 min. Factor 3 is fixed at the lower limit of the full factorial (i.e., temperatures of steps 1–3 in He: 125°C, 366°C, and 608°C), respectively.

in He was either 550°C (60% of variance) or 850°C (15% of variance), respectively. Figure 14 shows EC/TC as a function of the O₂-He step 1 duration, taken from the EC/TC response surface. In this case, the He step 4 temperature was 840°C. In the O₂-He phase, we are no longer concerned with the positive bias from uncharred OC. Thus, we seek a maximum in the EC response for this factor. For the three sample types, EC/TC increased with time. However, EC/TC for urban PM and smoldering fire emissions leveled off with time, while the ratio for lab air particles did not. A duration of 3 min for this step is sufficiently lengthy yet reasonable with respect to the overall time of analysis.

CONCLUSION

We have demonstrated the use of response surface modeling as a means to optimize the TOA temperature protocol for accurately measuring atmospheric EC as BC. The study was based on a central-composite factorial design consisting of four factors that considered the temperatures and durations of the four thermal desorption steps in TOA’s He phase and the initial step in TOA’s O₂-He phase. For the fourth step in He, temperatures and durations in the factorial design ranged from 500°C to 900°C and 1 min to 5 min. The temperature of this step accounted for the largest portion of variance by far in the factorial design. However, the duration of this step as well as the duration of the first O₂-He step had a significant effect on the EC/TC ratio, depending on the He step 4 temperature.

Our approach to optimizing TOA was based on two goals. First, we sought to minimize a positive bias from the detection of residual OC on the filter as native EC by maximizing the production OC char by the instrument. Second, we sought to minimize a negative bias from the loss of native EC at high temperatures. With these goals in mind, we modeled three variables based on instrument responses: EC/TC, maximum laser attenuation in He (L_{\max}), and laser attenuation at the end of the He phase (L_{He4}). A comparison of the EC/TC and L_{\max} surfaces revealed how OC char production and change in the He phase relates to EC/TC. TOA optimization is complicated by the fact that the loss of native EC at high temperatures in He occurs at the same time that OC charring increases. The intersection between the L_{\max} and L_{He4} surfaces for the three samples revealed the conditions in the He phase that minimize potential biases and thus led to an optimized thermal desorption protocol.

Table 6 presents the optimal TOA conditions based on samples used in this study. An instrument that monitors the change in sample transmission during analysis requires pre-specified step durations (i.e., TOT). However, the protocol may also be applicable to instruments that monitor sample reflectance (TOR) when step duration matches those in Table 6. The amount of total carbon on our samples was around 30 μg to 50 μg. Thus, the temperature protocol is applicable to similar samples in this carbon mass range. Our study indicated the following optimal temperatures, rounded to the nearest 5°C, and durations for steps

Table 6
Optimized thermal-desorption protocol for TOT using fixed-duration steps

	Step	Temperature (°C)	Duration (s)
He phase	1	190	60
	2	365	60
	3	610	60
	4	835	72
O ₂ -He phase (1% O ₂ v/v)	1	550	180
	2	700	60
	3	850	60
	4	900	90 to 120

1–4 in He: 190°C for 60 s, 365°C for 60 s, 610°C for 60 s, and 835°C for 72 s, respectively. These temperatures are lower than those associated with NIOSH 5040 but higher than the IMPROVE temperatures. For steps 1–4 in O₂-He we used 550°C for 180 s, 700°C for 60 s, 850°C for 60 s, and 900°C for 90 s to 120 s, depending on when the final O₂-He peak reaches baseline.

The TOA protocol presented here is not intended for all carbonaceous PM samples. Therefore, we recommend additional studies for optimizing TOA using factorial designs and response surface methods such as those presented here. These studies should involve ambient air samples impacted by varying PM source emissions and their aging, as well as different emission source samples themselves, including diesel emissions under varying load conditions. Additional response surface studies will likely lead to a more comprehensive understanding of TOA behavior as well as an assessment of how protocols may need to be fine-tuned for characteristically different types of carbonaceous PM.

REFERENCES

- Ackerman, T. P., and Toon, O. P. (1981). Absorption of Visible Radiation in Atmospheres Containing Mixtures of Absorbing and Non-Absorbing Particles, *Appl. Opt.* 20:3663–3998.
- Birch, M. E. (1998). Analysis of Carbonaceous Aerosols: Interlaboratory Comparison, *Analyst* 123:851–857.
- Birch, M. E. (1999). *Elemental Carbon (Diesel Particulate): Method 5040*, Issue 3 (Interim), NIOSH Manual of Analytical Methods, 4th ed., DHHS (NIOSH) Publication No. 94-113, M. E. Cassinelli and P. F. O'Connor, eds., National Institute for Occupational Safety and Health, U.S. Department of Health and Human Services, Cincinnati, OH.
- Birch, M. E., and Cary, R. A. (1996). Elemental Carbon-Based Method for Occupational Monitoring of Particulate Diesel Exhaust: Methodology and Exposure Issues, *Analyst* 121:1183–1190.
- Bond, T. C., Anderson, T. L., and Campbell, D. (1999). Calibration and Intercomparison of Filter-Based Measurements of Visible Light Absorption by Aerosols, *Aerosol Sci. Technol.* 30:582–600.
- Box, G. E. P., Hunter, W. G., and Hunter, J. S. (1978). *Statistics for Experimenters*, John Wiley & Sons, New York.
- Campbell, D., Copeland, S., and Cahill, T. (1995). Measurement of Aerosol Absorption-Coefficient From Teflon Filters Using Integrating Plate and Integrating Sphere Techniques, *Aerosol Sci. Technol.* 22:287–292.
- Cary, R. A. (1994). *Sunset Laboratory' Thermal Optical Analyzer Operating Manual*, Sunset Laboratory, Inc., Forest Grove, OR.
- Chow, J. C., Watson, J. G., Crow, D., Lowenthal, D. H., and Merrifield, T. (2001). Comparison of IMPROVE and NIOSH Carbon Measurements, *Aerosol Sci. Technol.* 34:23–34.
- Chow, J. C., Watson, J. G., Pritchett, L. C., Pierson, W. R., Frazier, C. A., and Purcell, R. G. (1993). The Dri Thermal Optical Reflectance Carbon Analysis System—Description, Evaluation and Applications in United-States Air-Quality Studies, *Atmos. Environ. Part A—General Topics* 27:1185–1201.
- Clarke, A. D. (1982). Integrating Sandwich—A New Method of Measurement of the Light-Absorption Coefficient for Atmospheric Particles, *Appl. Opt.* 21:3011–3020.
- Conny, J. M., and Slater, J. F. (2002). Black Carbon and Organic Carbon in Aerosol Particles from Crown Fires in the Canadian Boreal Forest, *J. Geophys. Res.—Atmos.* 107:10.1029/2001JD001528.
- Currie, L. A., Benner, B. A. Jr., Kessler, J. D., Klinedinst, D. B., Klouda, G. A., Marolf, J. V., Slater, J. F., Wise, S. A., Cachier, H., Cary, R., Chow, J. C., Watson, J., Druffel, E. R. M., Masiello, C. A., Eglinton, T. I., Pearson, A., Reddy, C. M., Gustafsson, Ö., Quinn, J. G., Hartmann, P. C., Hedges, J. I., Prentice, K. M., Kirchstetter, T. W., Novakov, T., Puxbaum, H., and Schmid, H. (2002). A Critical Evaluation of Interlaboratory Data on Total, Elemental, and Isotopic Carbon in the Carbonaceous Particle Reference Material, NIST SRM 1649a, *J. Res. Natl. Inst. Stand. Technol.* 107:279–298.
- Gundel, L. A., Dod, R. L., Rosen, H., and Novakov, T. (1984). The Relationship Between Optical Attenuation and Black Carbon Concentration for Ambient and Source Particles, *Sci. Total Environ.* 36:197–202.
- Hansen, A. D. A., Rosen, H., and Novakov, T. (1984). The Aethalometer—An Instrument for the Real-Time Measurement of Optical-Absorption by Aerosol-Particles, *Sci. Total Environ.* 36:191–196.
- Hitzenberger, R. (1993). Absorption Coefficients and Mass Concentrations in the Urban Aerosol of Vienna, Austria, During the Years 1985 and 1986, *Water Air Soil Pollut.* 71:131–153.
- Hitzenberger, R., Dusek, U., and Berner, A. (1996). Black Carbon Measurements Using an Integrating Sphere, *J. Geophys. Res.—Atmos.* 101:19601–19606.
- Hopper, J. F., Worthy, D. E. J., Barrie, L. A., and Trivett, N. B. A. (1994). Atmospheric Observations of Aerosol Black Carbon, Carbon-Dioxide, and Methane in the High Arctic, *Atmos. Environ.* 28:3047–3054.
- Huntzicker, J. J., Johnson, R. L., Shah, J. J., and Cary, R. A. (1982). Analysis of Organic and Elemental Carbon in Ambient Aerosol by a Thermal-Optical Method, in *Particulate Carbon: Atmospheric Life Cycle*, G. T. Wolff and R. L. Klimish, eds., Plenum Press, New York, pp. 79–88.
- ISO (1993). *Guide to the Expression of Uncertainties in Measurement*, International Organization for Standardization, Geneva, Switzerland.
- Johnson, R. L., Shah, J. J., Cary, R. A., and Huntzicker, J. J. (1981). An Automated Thermal-Optical Method for the Analysis of Carbonaceous Aerosol, in *Atmospheric Aerosol: Source/Air Quality Relationships*, E. S. Macias and P. K. Hopke, eds., American Chemical Society, Washington, D. C., pp. 223–233.
- Klouda, G. A. (2002). Personal Communication.
- Klouda, G. A., Parish, H. J., Klinedinst, D. B., Steel, E. B., and Benner, Jr., B. A. (1996). Exploring a Method to Produce an Urban Dust Particle Filter Standard, *J. Aerosol Sci.* 27:S351–S352.
- Lin, C.-I., Baker, M., and Charlson, R. J. (1973). Absorption Coefficient of Atmospheric Aerosol: A Method of Measurement, *Appl. Opt.* 12:1356–1362.
- Malm, W. C., Sisler, J. F., Huffman, D., Eldred, R. A., and Cahill, T. A. (1994). Spatial and Seasonal Trends in Particle Concentration and Optical Extinction in the United States, *J. Geophys. Res.—Atmos.* 99:1347–1370.
- Massart, D. L., Vandeginste, B. G. M., Deming, S. N., Michotte, Y., and Kaufman, L. (1988). *Chemometrics: A Textbook*, Elsevier, Amsterdam.
- NIST (2001). *National Institute of Standards and Technology Certificate of Analysis*, Standard Reference Material 1649a, (Urban Dust), National Institute of Standards and Technology, Gaithersburg, MD.
- Novakov, T., and Corrigan, C. E. (1995). Thermal Characterization of Biomass Smoke Particles, *Mikrochimica Acta* 119:157–166.

- Pope, C. A., Burnett, R. T., Thun, M. J., Calle, E. E., Krewski, D., Ito, K., and Thurston, G. D. (2002). Lung Cancer, Cardiopulmonary Mortality, and Long-Term Exposure to Fine Particulate Air Pollution, *JAMA* 287:1132–1141.
- Savitzky, A., and Golay, M. J. E. (1964). Smoothing and Differentiation of Data by Simplified Least Squares Procedures, *Anal. Chem.* 36:1627–1639.
- Seinfeld, J. H., and Pandis, S. N. (1998). *Atmospheric Chemistry and Physics*. John Wiley and Sons, New York, pp. 700–765.
- Shi, J. P., Mark, D., and Harrison, R. M. (2000). Characterization of Particles From a Current Technology Heavy-Duty Diesel Engine, *Environ. Sci. Technol.* 34:748–755.
- Taylor, B. N., and Kuyatt, C. E. (1994). *Guidelines for Evaluating and Expressing the Uncertainty of NIST Measurement Results*, NIST Technical Note 1297, National Institute of Standards and Technology, Gaithersburg, MD.
- Watson, A. Y., and Valberg, P. A. (2001). Carbon Black and Soot: Two Different Substances, *AHJAJ* 62:218–228.
- Wolff, E. W., and Cachier, H. (2002). Concentrations and Seasonal Cycle of Black Carbon in Aerosol at a Coastal Antarctic Station, *J. Geophys. Res.* 103:11033–11041.
- Xiong, C., and Friedlander, S. K. (2001). Morphological Properties of Atmospheric Aerosol Aggregates, *Proceedings of the National Academy of Sciences of the United States of America* 98:11851–11856.